A Study and Modelling of Chaff Clouds Affected by Wing-Tip Vortices

Jonathan Persson
ast13jpe@student.lu.se
Jakob Warlin
tfy13jwa@student.lu.se

Department of Electrical and Information Technology
Lund University

Supervisors: Daniel Sjöberg (LTH)
Albert Nummelin (SAAB Surveillance)

Examiner: Mats Gustafsson

May 14, 2019

Printed in Sweden
Tryckeriet i E-huset, Lund

Abstract

Chaff are thin strips of either metal or metal coated fibres used as countermeasures against radar. When deployed from an airplane, the turbulence and wing-tip vortices from the airplane disperse the chaff into a chaff cloud, which may appear as a false target and jam the radar. A Doppler radar is able to discriminate between chaff and targets by using the Doppler spectra. Such signal processing methods already exist, and are evaluated with real data from flight tests. However, flight tests are expensive and a way to simulate a chaff cloud would therefore be preferred.

This master thesis was a pilot study which investigated the current knowledge of chaff modelling with wing-tip vortices. Two models were created, an individual chaff model and a Gaussian model. The individual chaff model was based on physical phenomena and simulated the effect of the wing-tip vortices on a chaff cloud. The Gaussian model was based on distributions and trends, and should be adjusted to real data. Due to confidentiality, real data could not be used. Instead, two flight scenarios were used to evaluate the individual chaff model. The Gaussian model was then adapted to these results.

The individual chaff model was able to simulate two separate flight scenarios with distinguishable results. Moreover, the model also showed some promising results when compared to RCS trends from previous published models. Statistical characteristics of the RCS values agreed with Swerling models. The RCS values were however low, due to insufficient diffusion simulation. This also resulted in inaccurately simulated cloud sizes. The Gaussian model was able to mimic the behaviour of the individual chaff model with reduced run-time.

More work is necessary to fully understand the behaviour of wing-tip vortices, as well as the ability to use real data for evaluation. Theoretical work and more advanced simulation methods are required to understand and model the behaviour properly.

Acknowledgements

Firstly, we would like to thank our supervisors at SAAB Surveillance, Dennis Sångberg, Alexandra Andersson and Albert Nummelin, and our supervisor at LTH, Daniel Sjöberg, for their guidance and support throughout our master thesis. We would also like to thank Roger Larsson and Alf Näsvall for theoretical assistance regarding aerodynamics and chaff modelling. Finally, we would like to thank Magnus Enger for giving us the opportunity to conduct our master thesis at SAAB Surveillance in Gothenburg.

Contents

Chapter 1
Introduction

1.1 Background and Motivation

Modern fighter airplanes are equipped with radars, and countermeasure systems used to jam enemy radar. The main objective of the radar is to search for new targets and keep track of known targets, and then transfer the target data to a radar-guided missile. There are two types of radar countermeasures, active and passive jamming. Active jamming includes radiating high power noise or other forms of electromagnetic waves which actively disrupt the enemy radar. Passive jamming uses devices to reflect radar energy and create false targets.

A common passive radar countermeasure is chaff. Chaff are very thin strips of metal or metal coated fibres, as seen in figure 1.1. The length of chaff are adapted to radar wavelengths and one package usually contains many different lengths to counteract multiple radar frequencies. When chaff are deployed, they create a cloud which may be perceived as a real target and jam enemy radar. Chaff are usually distributed pyrotechnically, or by the aerodynamic turbulence from the airplane [1].

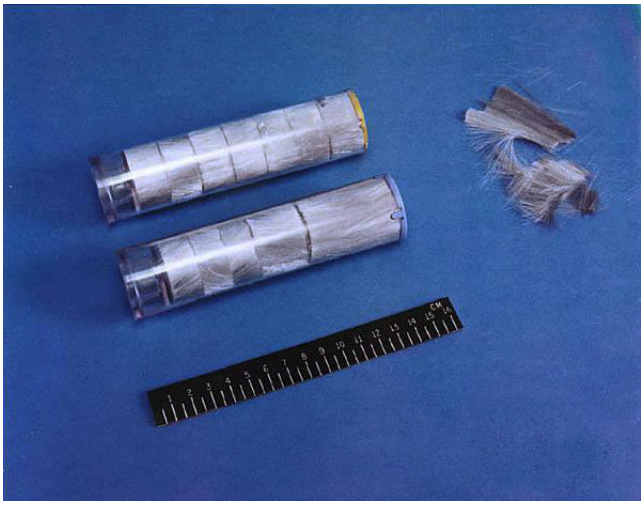

Figure 1.1: Chaff in container [2].

Chaff should not be confused with flares, which might be the more well known, and visually impressive, countermeasure. Flares are countermeasures used against heat-seeking missiles and not against radar. In comparison, chaff are barely visible when deployed [3].

Figure 1.2: Flares deployed from a C-130 Hercules [4].

The wing-tip vortices help disperse the chaff behind the airplane and create a cloud with a large surface area and volume. This cloud reflects radar waves and can be mistaken for a real target by enemy radar and radar-guided missiles, see figure 1.3.

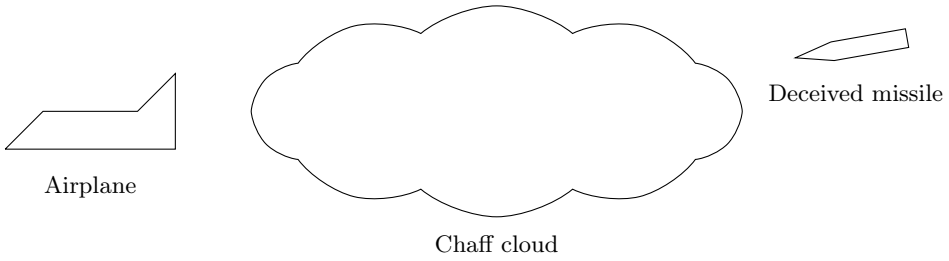

Figure 1.3: Chaff clouds create a fake target which radar and radar-guided missiles may mistake for a real target.

In a modern pulse-Doppler radar, there are several different signal processing methods to distinguish real targets from chaff. One method is to analyse the Doppler spectra. When the chaff are affected by turbulence and wing-tip vortices, the resulting chaff cloud have a larger variation of velocities than the airplane. The chaff velocities will quickly decrease and converge to the wind velocities. Therefore,

the chaff Doppler spectrum will be different from the airplane's. Flight tests are usually conducted to try such methods, which require a lot of time and resources. It would therefore be better to simulate the distribution of chaff in the presence of wing-tip vortices.

1.2 Project Goals

The goals for this master thesis project are:

- Conduct a literature study to investigate existing chaff models including the effect of wing-tip vortices.
- Create a model in MATLAB simulating the aerodynamic and spectral characteristics of a chaff cloud.
- The model should generate input to existing signal processing methods that analyse Doppler spectra of chaff clouds.

1.3 Outline

The outline of this thesis is as follows: Chapter 1 introduces the subject and project goals. Chapter 2 explains relevant radar and aerodynamic concepts useful for the thesis. The literature study in chapter 3 investigates previous work on chaff models and the known physical understanding of wing-tip vortices. With this knowledge in mind, chapter 4 describes the simulation process for the models. Chapter 5 presents the results from conducted simulation tests as well as the discussion. Proposed improvements for the models are presented in future work in chapter 6. Lastly, conclusions are drawn in chapter 7.

Chapter 2
Theory

This chapter covers many of the radar concepts used throughout the rest of the thesis, such as the radar equation, radar cross section and range-Doppler plots. Moreover, this section also covers some theory on chaff and aerodynamics. The chaff section introduces some known chaff characteristics and modelling approaches while the aerodynamics focuses on the drag equation and wing-tip vortices.

2.1 Radar

Radar (Radio Detection And Ranging) is a system that uses electromagnetic waves, specifically radio waves, to detect objects. A basic radar consists of a transmitter, a receiver, two antennas and a display. The transmitter uses one of the antennas to emit radio waves. These waves are then reflected by the target, creating radar echoes, which can be detected by the receiver antenna. It is common that the receiver and the transmitter share the same antenna and take turns using it to avoid interference. Such a radar is called a pulsed radar and emits pulses of radio waves with a specific transmit time and a specific pulse repetition frequency (PRF). The PRF is the inverse of the time between transmitted pulses, which is called the pulse repetition interval (PRI). In-between pulses, the radar listens for pulse echoes. This time is called listening time. The return time is the time between the transmitted pulse and the pulse echo, see figure 2.1 [5, ch. 1].

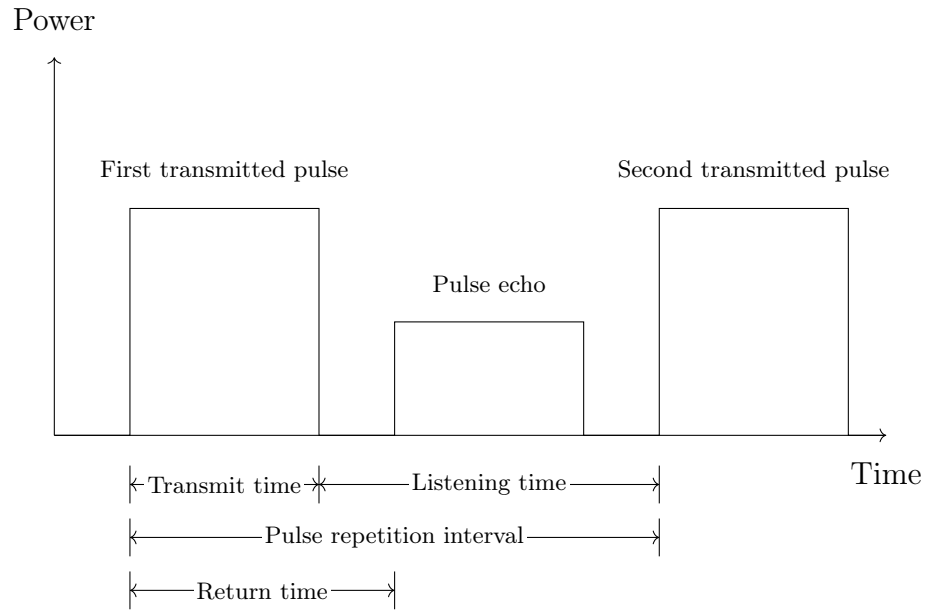

Figure 2.1: Definition of pulse width, listening time, pulse repetition interval and return time.

The distance to a target can be determined by measuring the return time using [5, ch. 12],

$$R = c \cdot \frac{t_{\mathrm{d}}}{2}, \tag{2.1}$$

where
R = distance to target [m]
c = speed of light [m/s]
t_{d} = return time [s].

If the pulse echo in figure 2.1 appears after the second transmitted pulse it is not certain which pulse the echo belongs to, thus the range cannot be uniquely determined. This is called range ambiguity and is related to the choice of PRF. The relationship between the PRF and the maximum unambiguous range is given by [5, ch. 12],

$$\text{Maximum unambiguous range} = \frac{c}{2 \cdot \mathrm{PRF}}. \tag{2.2}$$

The range-rate (radial velocity relative to the radar) of the target can be determined by examining the frequency shift f_{D} of the pulse echo caused by the Doppler effect [5, ch. 15],

$$f_{\mathrm{D}} = -2\frac{\dot{R}}{\lambda}, \tag{2.3}$$

where
f_{D} = Doppler shift in frequency [Hz]

$\dot{R}$ = range-rate [m/s]
λ = radar transmitted wavelength [m].

2.1.1 Radar Equation

The received signal power returned from a target can be calculated with the radar equation [6, ch. 1],

$$P_{\mathrm{r}} = \frac{P_{\mathrm{t}} G_{\mathrm{t}} G_{\mathrm{r}} \sigma \lambda^2}{(4\pi)^3 R^4}, \tag{2.4}$$

where
P_{r} = received signal power [W]
P_{t} = peak transmitted power [W]
$G_{\mathrm{t}}, G_{\mathrm{r}}$ = transmitted and received antenna gain [-]
σ = target radar cross-section [m^2]
λ = radar wavelength [m]
R = distance to target [m].

The radar cross-section (RCS) is a measure determining how detectable an object is by radar. It is determined by three factors; the geometric cross-section, the reflectivity and the directivity. The geometric cross-section is defined as the cross-sectional area viewed by the radar. Reflectivity determines how much of the transmitted radar energy is scattered by the object, i.e. re-radiated. Lastly, the directivity decides how much of the scattered power reaches the radar. The RCS, denoted σ, is given by [5, ch. 10],

$$\sigma = \text{Geometric Cross-Section} \times \text{Reflectivity} \times \text{Directivity}. \tag{2.5}$$

The returned signal from a point target can be described as [7, 8],

$$x(t) \sim \sqrt{P_{\mathrm{r}}} \cdot s(t - t_{\mathrm{d}}) e^{-j2\pi f_{\mathrm{D}} t} e^{j\psi} \tag{2.6}$$

where
$x(t)$ = received signal [V]
P_{r} = received signal power [W]
$s(t)$ = transmitted pulse, normalised with peak amplitude [-]
t_{d} = time delay from transmission to reception [s]
f_{D} = Doppler frequency shift [Hz]
ψ = random phase due to interaction with target [-].

(2.6) includes a time delay, t_{d}, described in (2.1), a Doppler shift, f_{D}, from (2.3) and an amplitude proportional to the square root of the received power P_{r} from (2.4).

The pulses are often sent in bursts consisting of a couple of hundred pulses. An entire burst is described by,

$$x_{\mathrm{tot}}(t) = \sum_{k=0}^{N_{\mathrm{pri}}-1} x(t - k t_{\mathrm{pri}}), \tag{2.7}$$

where
$x_{\text{tot}}(t)$ = echo of a burst [V]
N_{pri} = number of pulses in the burst [-]
t_{pri} = pulse repetition interval [s].

The received data from a burst echo is often stored in a matrix, where each column consists of a single sampled pulse, and the number of columns represents the number of pulses in the burst. This can be visualized by a burst plot, as seen in figure 2.2. The y-axis is called fast time and shows the sampled time in a pulse whereas the x-axis is called slow time and shows the pulse number. The time between each pulse is the PRI of the radar. The PRI used in the figure is $984 \cdot 10^{-7}$ s, which gives a maximum unambiguous range of roughly 14.75 km.

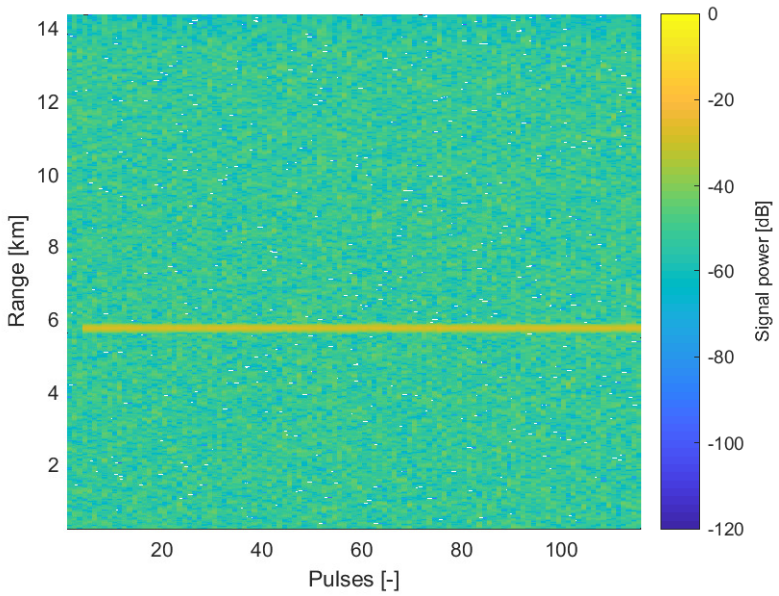

Figure 2.2: Burst plot of a point target at range 50 km with a range-rate of 520 m/s. Due to range ambiguity, the target appears to be at roughly 6 km. The fast time has been converted to range using (2.1).

From (2.6) and (2.7), each pulse will experience a phase shift originating from the term $e^{-j2\pi f_{\mathrm{D}} k t_{\mathrm{pri}}}$, where k is the pulse number. Since the x-axis is sampled at times kt_{pri}, this can be seen as a frequency of f_{D} along this axis. This frequency can be found by using discrete FFT on each row in the matrix, and since f_{D} is the Doppler frequency of the target, this also gives the velocity components of the target, as given by (2.3). The result is often shown in a range-Doppler plot, which can be seen for a point target in figure 2.3 [8].

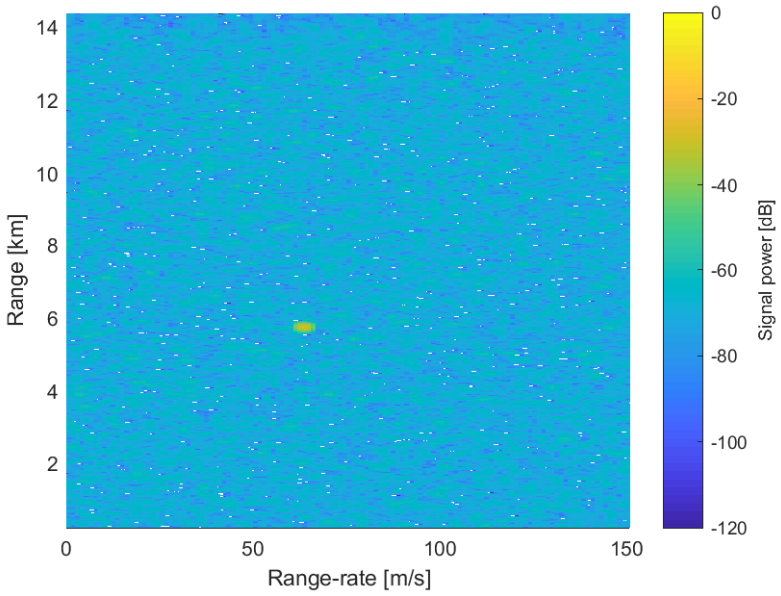

Figure 2.3: Range-Doppler plot of a point target at range 50 km with a range-rate of 520 m/s. The PRI is $984 \cdot 10^{-7}$ s.

Similar to range ambiguity, there is also a Doppler ambiguity caused by aliasing. The sampling frequency is in this case the radar PRF which represents a maximum unambiguous range-rate of roughly 150 m/s. This can be seen in figure 2.3, where the actual range-rate of the target is 520 m/s but the signal has folded three times and appears to be at $520 - 3 \cdot 150 = 70$ m/s. This problem can be solved by using a PRF high enough to cover the target range-rate. This would however cause the range to be ambiguous. Due to this dilemma, the types of PRF used in radars are often categorized as either low (LPRF), medium (MPRF) or high (HPRF). LPRF denotes a PRF for which the maximum range the radar is supposed to handle is unambiguous, HPRF denotes the PRF for which the expected Doppler shifts are unambiguous and MPRF denotes the PRF that are neither high nor low. The simulated radar in figure 2.3 uses an MPRF.

2.2 Chaff

Chaff as a radar countermeasure has been used ever since the Second World War. They were first used as a countermeasure by the British during a bombing raid on Hamburg in 1943. Metal foil was cut into strips with dimensions of 15mm x 300mm and divided into packages of about 1000 strips each. They turned out to be very effective against the German radars Wurzburg (570 MHz) and Lichtenstein (490 MHz) [9].

Nowadays, chaff are usually made of dielectric fibres, like nylon or glass, with a metal coating of typically silver or aluminium. It is still a common countermeasure even though other countermeasures have been developed, mainly because of its simplicity. When the radar waves interact with the chaff, they resonate and the waves are reflected back to the radar. The ideal length of a strip is half the length of the enemy radar wavelength, as this gives maximum resonance. Since the frequency used by the enemy radar is unknown, a batch of chaff often contains different lengths to counter a larger range of radars using different wavelengths. Chaff are released from containers usually located under the wings of an airplane, and are dispersed by the turbulence and wing-tip vortices. Due to their tiny weight ($\approx 27.5 \cdot 10^{-9}$ kg [10, p. 7]), the chaff quickly react to the turbulent winds and create a large cloud. This cloud can then act as a false target to cover the airplane and jam the enemy radar, and potentially break the lock of a radar-guided missile [5, ch. 34].

2.2.1 RCS of Chaff Clouds

Due to the incoherence of the waves reflected from each individual chaff, the average RCS of a chaff cloud can be calculated as the average RCS of a single chaff times the number of operational chaff in the cloud [1, ch. 5],

$$\bar{\sigma}_{\text{cloud}} = \mu N \bar{\sigma}_{\text{chaff}}, \tag{2.8}$$

where

$\bar{\sigma}_{\text{cloud}}$ = average RCS of a chaff cloud [m^2]
μ = percentage of operational chaff [-]
N = total number of chaff [-]
$\bar{\sigma}_{\text{chaff}}$ = average RCS of a single chaff [m^2].

The number of operational chaff is usually about 50% to 65% of the total number due to them sticking together and breaking [6, p. 262]. Another phenomenon affecting the RCS of a cloud is mutual coupling. Mutual coupling is an often undesirable electromagnetic interaction which can occur between closely spaced antennas. The energy transmitted from an antenna is partly absorbed by the other antennas, reducing the total antenna efficiency. A similar effect also occurs in a chaff cloud between different scattering chaff particles which reduces the RCS [11]. This effect is negligible if the average spacing between chaff is larger than two wavelengths, and is often ignored in chaff models [12].

Due to the chaotic nature of the aerodynamics behind an airplane, it is hard to determine the directions of chaff in a cloud and it is therefore common to assume

a uniform distribution of orientations. The average RCS of a single chaff with a length equal to half the radar wavelength is then given by [1, ch. 5],

$$\bar{\sigma}_{\text{chaff}} = 0.17\lambda^2, \tag{2.9}$$

where
λ = wavelength of the radar [m].

The measured RCS values will however fluctuate around the average due to the interference between different chaff echoes. The effective RCS as seen by the radar at a specific point in time can be written as [13],

$$\sigma_{\text{effective}} = \left| \sum_{k=1}^{N} \sqrt{\sigma_k} e^{-j4\pi R_k/\lambda} \right|^2, \tag{2.10}$$

where
N = the number of chaff in the cloud [-]
σ_{k} = RCS of chaff k [m^2]
R_{k} = range to chaff k [m].

The statistical properties of the effective RCS for different complex targets can be described with Swerling target models. Swerling 1 and Swerling 2 are based on a target consisting of many similar individual scatterers, such as in a chaff cloud, and describe the RCS as an exponential distribution [13],

$$P(\sigma) = \frac{1}{\sigma_{\text{avg}}} e^{(-\frac{\sigma}{\sigma_{\text{avg}}})}, \quad \sigma > 0, \tag{2.11}$$

where
σ_{avg} = average RCS of the cloud [m^2].

The difference between Swerling 1 and Swerling 2 is whether the measured RCS value varies from scan to scan or from pulse to pulse.

2.2.2 Chaff Cloud Dynamics

The stages of chaff dispersion after drop can be categorised into three phases: the blooming phase, the mature phase and the decay phase. The blooming phase involves the release of chaff and their quick dispersion by the turbulence and wing-tip vortices, and lasts for a few seconds. During the mature phase, the chaff cloud reaches its maximum RCS which remains more or less constant and the velocities in the cloud are determined mostly by the weather conditions. The chaff then slowly moves towards the ground during the decaying phase [14]. Typical sizes of chaff clouds at different times can be seen in table 2.1 [15]:

Time	Width	Height
50 ms	3-5 m	1-2 m
100 ms	4-6 m	3-4 m
60 s	10-20 m	20-40 m

Table 2.1: Typical chaff cloud sizes at specific times after drop.

The dynamics of a chaff cloud can be described as chaff particles drifting randomly in three dimensions. This results in a convection-diffusion equation describing the probability density for the chaff cloud. In one dimension, this can be written as [1, ch. 5],

$$\frac{\partial p}{\partial t} = -A_x \frac{\partial p}{\partial x} + \frac{1}{2} B_x \frac{\partial^2 p}{\partial x^2}, \tag{2.12}$$

where
$p(x,t)$ = probability density at position x at time t [1/m]
A_x = drift coefficient [m/s]
B_x = diffusion coefficient [m^2/s].

Assuming the concentration is initially focused in a point x_0, i.e. using the initial condition $p(x,0) = \delta(x - x_0)$, and assuming that the coefficients are constant, the solution can be written as a Gaussian distribution [1, ch. 5],

$$p(x,t) = \frac{1}{\sqrt{2\pi B_x t}} \exp\left(-\frac{(x - A_x t)^2}{2B_x t}\right). \tag{2.13}$$

In three dimensions, the convection-diffusion equation can be written as [16],

$$\frac{\partial p}{\partial t} = -A_x \frac{\partial p}{\partial x} - A_y \frac{\partial p}{\partial y} - A_z \frac{\partial p}{\partial z} + \frac{\partial}{\partial x}\left(D_x \frac{\partial p}{\partial x}\right) + \frac{\partial}{\partial y}\left(D_y \frac{\partial p}{\partial y}\right) + \frac{\partial}{\partial z}\left(D_z \frac{\partial p}{\partial z}\right), \tag{2.14}$$

where
$A_x,\ A_y,\ A_z$ = velocities along the x-, y- and z-axis [m/s]
$D_x,\ D_y,\ D_z$ = diffusion coefficients along the x-, y- and z-axis [m^2/s].

Note that (2.12) and (2.14) are taken from different sources and use different conventions for the diffusion coefficients, D_x is the same as $\frac{1}{2}B_x$.

2.2.3 Chaff Doppler Spectrum

In the horizontal plane, chaff move with the wind similar to precipitation. The Doppler spectrum depends primarily on four different factors: wind shear, beam broadening, turbulence and different chaff falling velocities. The spectrum is often assumed to be normally distributed with a variance given by the sum of each factor [6, ch. 6],

$$\sigma^2 = \sigma^2_{\text{shear}} + \sigma^2_{\text{beam}} + \sigma^2_{\text{turb}} + \sigma^2_{\text{fall}}, \tag{2.15}$$

where
σ_{shear} = standard deviation from wind shear [m/s]
σ_{beam} = standard deviation from beam broadening [m/s]
σ_{turb} = standard deviation from turbulence [m/s]
σ_{fall} = standard deviation from different falling velocities [m/s].

Wind shear is a variation in wind speed with altitude. This effect is dependent on the beam width of the radar and is typically larger for ground-based radars. If the wind speed is assumed to increase linearly along the vertical axis with a constant gradient k, the contribution to the standard deviation can be approximated as [6, ch. 6],

$$\sigma_{\text{shear}} = 0.42kR\phi_2, \tag{2.16}$$

where
k = velocity gradient [m/s/km]
R = slant range to the cloud [km]
ϕ_2 = two-way, half power antenna elevation beamwidth [rad].

Beam broadening is the velocity spread coming from transforming wind velocities to radial components as seen by the radar. A velocity perpendicular to the beam center will have small radial components at the edges of the beam due to a difference in angles from the center. The standard deviation from this is given by [6, ch. 6],

$$\sigma_{\text{beam}} = 0.42V_0\theta_2 \sin\beta, \tag{2.17}$$

where
V_0 = range-rate at beam centre [m/s]
θ_2 = two-way, half power beamwidth of the antenna in azimuth [rad]
β = azimuth angle relative to wind direction at beam centre [rad].

The chaff are affected both by jet turbulence, caused by the airplane releasing the chaff, as well as atmospheric turbulence. The standard deviation component from atmospheric turbulence has been measured to be about 0.7 m/s on average above 12000 ft and 1.0 m/s below [6, ch. 6].

The final component is due to different falling velocities of chaff. There have been several studies measuring these velocities, and the standard deviation can in general be approximated as [6, ch. 6],

$$\sigma_{\text{fall}} = \sin\Psi, \tag{2.18}$$

where
Ψ = elevation angle of the beam [rad].

2.3 Aerodynamics and Wing-Tip Vortices

The main forces acting on an airplane are thrust, lift, weight and drag, see figure 2.4.

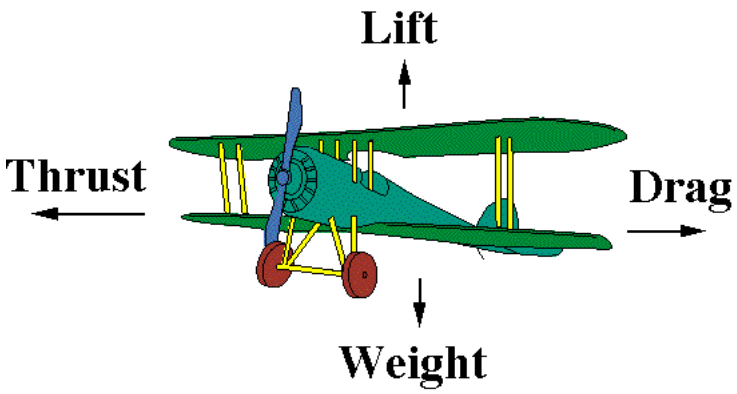

Figure 2.4: Forces acting on an airplane [17].

To be able to fly, an airplane needs to generate enough lift to overcome the weight. Lift is generated by the thrust and the shape of the wings, which are designed to create a pressure under the wings when the airplane is in motion, thus lifting it from the ground. Thrust is the force generated by the engines to overcome the drag and produce lift. Weight is the force acting on the plane due to its mass. When the airplane is moving, the drag force resists the motion, similar to friction. The overall drag force is a summary of different drag forces caused by multiple factors and is highly dependent on the airframe of the airplane. Similarly, the lift force also depends on the airframe, especially the design of the wings [18].

2.3.1 Calculating Lift

The force L required to lift an airplane is given by [19],

$$L = nmg, \tag{2.19}$$

where
n = load factor [-]
m = mass of the airplane [kg]
g = gravitational acceleration [m/s^2].

Increasing the load factor will require more lift. When an airplane turns, the load factor increases as well as the angular displacement, called bank, see section 2.3.2. A typical turn for a fighter airplane is a 3g turn, which corresponds to a load factor n of 3. The relationship between the load factor and the banking angle ϕ is [20, p. 407],

$$n = \frac{1}{\cos\phi}. \tag{2.20}$$

2.3.2 Flight Dynamics

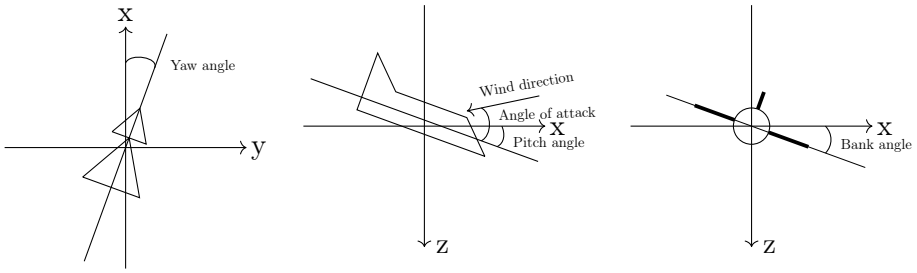

Figure 2.5: Definitions of yaw, pitch and bank angle as well as angle of attack.

Figure 2.5 shows the definitions of the yaw, pitch and bank angle of an airplane, and angle of attack. The pitch and bank angle are defined as the angular displacements around the horizontal and vertical axis, respectively. The angular displacement around the axis orthogonal to both these axes is called the yaw angle. Lastly, the angle of attack is defined as the angle between the direction of the airplane and the wind direction [20, ch. 16.6] [21].

2.3.3 Drag and the Drag Equation

Drag is a force acting on objects moving in a fluid, counteracting the forward motion, similar to friction. Every part of an airplane contributes to the total drag force. Drag is divided into multiple categories, for example skin-friction drag, which is generated by the friction between the surface and the fluid, wave drag due to shock waves in high-speed flight, induced drag due to wing-tip vortices, and more [22]. The drag for an object is given by the drag equation [23],

$$F_{\mathrm{D}} = \frac{1}{2}\rho v^2 C_{\mathrm{D}} A, \tag{2.21}$$

where

ρ = mass density of the fluid [kg/m^3]
v = speed of the object relative to the fluid [m/s]
C_{D} = drag coefficient [-]
A = cross-sectional area [m^2].

C_{D} incorporates different complex dependencies for the specific object into a single variable. For a chaff strip it is assumed to be the same as for a horizontally oriented infinite cylinder [10, p. 9],

$$C_{\mathrm{D}} = 10.5 \cdot R^{-0.63},\ 0.5 \leq R \leq 10. \tag{2.22}$$

The Reynolds number R is given by,

$$R = \frac{W_{\mathrm{T}} D \rho_{\mathrm{air}}}{\mu}, \tag{2.23}$$

where
W_T = terminal velocity [m/s]
D = chaff diameter [m]
ρ_{air} = air density [kg/m^3]
μ = dynamic viscosity of air [kg/m/s].

2.3.4 Wing-Tip Vortices

Airplane wings are shaped to create a higher pressure below than above, which generates lift. The pressure is equalised at the end of the wings, resulting in wing-tip vortices, sometimes called wake vortices, as seen in figure 2.6. The strength of the wake turbulence, and consequently the wing-tip vortices, depends primarily on the speed, weight and wingspan of the airplane. The flight configuration and design of the airplane has a lesser impact [24].

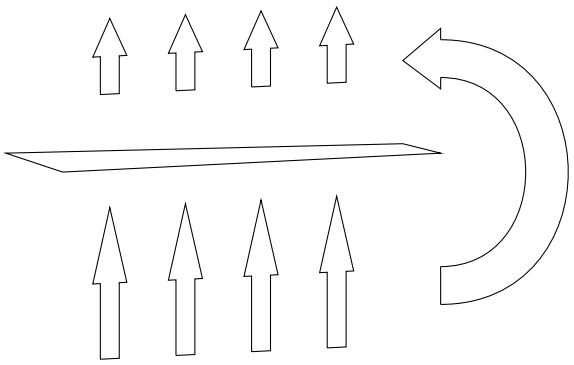

Figure 2.6: The shape of wings results in a higher pressure below than above. The pressure is equalised at the wing-tips, resulting in wing-tip vortices.

The vortices result in trailing tip vortices behind the airplane. They can linger for several minutes in the air, causing problems for other airplanes and at airports. Smaller airplanes in particular may lose control if caught in vortices from a larger airplane. Multiple smaller vortices are created from a wing and vortices with the same direction of circulation combine into larger vortices, conserving the total vorticity. The result is two large vortices, one from each wing. This happens during the so called roll-up phase, see figure 2.7. Vortices may also be created from other parts of the airplane, depending on the shape of the airframe and the wing design [24].

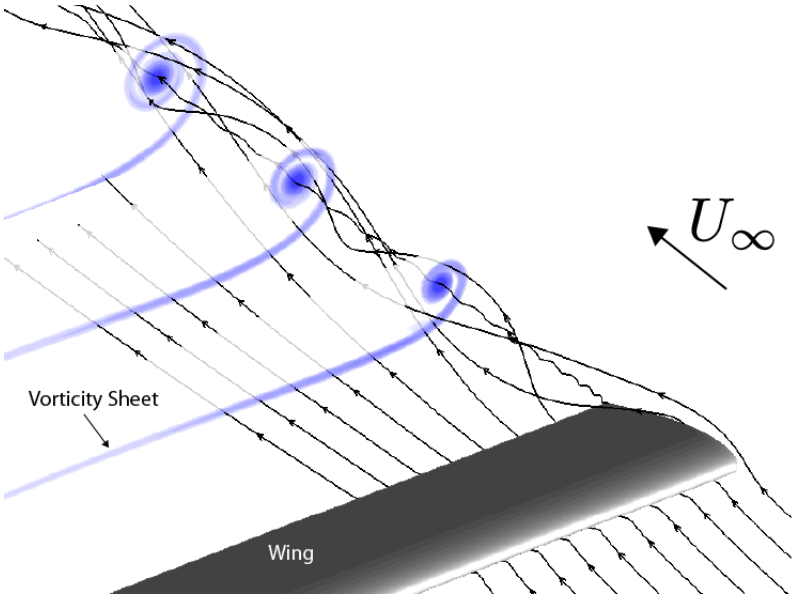

Figure 2.7: Small vortices roll up into two large vortices, one from each wing, during the roll-up phase [25].

Chapter 3
Literature Study

The following chapter investigates previous work on chaff models and the known physical understanding of wing-tip vortices. It starts by introducing some chaff models without any interaction with wing-tip vortices. The aerodynamics section then describes how the wing-tip vortices are created and some of their characteristics. Lastly, previous work done at SAAB as well as existing models where chaff clouds are combined with wing-tip vortices are presented.

3.1 Chaff models

3.1.1 P. Puoliguen

In [26], Puoliguen et al. describe a software called SILEM developed for the French Ministry of Defence in order to simulate chaff clouds dropped from battleships in naval situations. The software uses a model where the chaff concentration at all times is given by a three-dimensional Gaussian distribution with time varying means and standard deviations,

$$c_i(x,y,z) = \frac{m_i}{(2\pi)^{3/2}\sigma_x\sigma_y\sigma_z} e^{-\left[\frac{(x-\mu_x)^2}{2\sigma_x^2}+\frac{(y-\mu_y)^2}{2\sigma_y^2}+\frac{(z-\mu_z)^2}{2\sigma_z^2}\right]}, \tag{3.1}$$

where

m_i = total mass for chaff cloud i [kg]
$\mu_x,\ \mu_y,\ \mu_z$ = the cloud centre coordinates [m]
$\sigma_x,\ \sigma_y,\ \sigma_z$ = standard deviations along $x,\ y,\ z$ coordinates [m].

During simulation, the cloud centre is updated based on wind velocity. The standard deviations are updated differently depending on two phases; during the forced initial conditions right after ejection and during weather conditions.

The scattering characteristics of the cloud are simulated by dividing the cloud into 3D segments in a spherical grid originating from the radar position. The grid is used to construct an impulse response of the chaff cloud but also to take antenna gain in different directions into account. Furthermore, the orientations of the chaff are assumed to be distributed in two preferential groups, close to vertical and horizontal orientations. Based on these assumptions, the average RCS of a

chaff strip is calculated and the total RCS of the entire cloud is approximated as the mean RCS multiplied with the number of chaff in the cloud.

3.1.2 D. D. Ducata

Another approach is presented in [27], where D. D. Ducata suggests a model describing the kinematic, statistical and non-stationary behaviour of chaff. The model is based on a trend to simulate the RCS growth over time $f(t)$ in three different phases, described in (3.2). The trend uses an exponential function during the first phase, a constant value during the second phase and an arctangent function during the third phase,

$$f(t) = \begin{cases} 1 - \exp(-t/\tau_\mathrm{c}), & t \leq \tau \\ 1, & \tau < t \leq \tau_\mathrm{IF} \\ \frac{1}{2} - \frac{1}{\pi}\arctan(t - \tau_\mathrm{IF} - \Delta), & \tau_\mathrm{IF} < t \leq \tau_\mathrm{EF}, \end{cases} \tag{3.2}$$

where
τ_c = exponential constant [s]
τ = end time for exponential phase [s]
τ_IF = end time for second phase [s]
Δ = trend constant for the arctangent phase [s]
τ_EF = end time for arctangent phase [s].

The trend is then multiplied with the average cloud RCS calculated similarly to (2.8) and (2.9) with $\mu = 1$. Furthermore, the RCS is assumed to follow an exponential distribution, similar to the Swerling target models in (2.11). The spectral density in the model is assumed to be normally distributed with a standard distribution dependent on various components such as wind shear, beam broadening, wind turbulence and fall velocities, as described in section 2.2.3. The purpose of the model is to be useful in both avionic and naval scenarios, and can also account for bistatic radars by weighting the RCS values. A plot of the trend in (3.2) can be seen in figure 3.1.

3.1.3 U. Kaydok

U. Kaydok proposes a model similar to the one by D. D. Ducata in [28], where the same RCS trend, Swerling model and spectral density distribution are used. The model further assumes the shape of the cloud to be an oblate spheroid, with a volume described by,

$$V = \frac{4}{3}\pi r_\mathrm{a}^2 r_\mathrm{c}, \tag{3.3}$$

where
r_a = radius in horizontal plane [m]
r_c = vertical radius [m].

The horizontal radius r_a is assumed to be related to the RCS of the cloud and follow the square root of the trend in (3.2), multiplied with the maximum cloud radius r_max, while the vertical radius is assumed to remain constant.

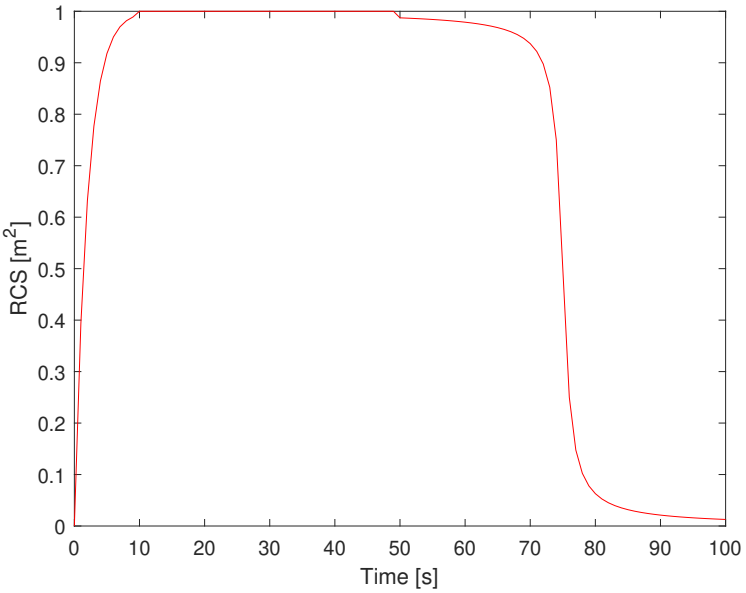

Figure 3.1: Plot of the trend in 3.2 where τ_C = 2 s, τ = 10 s, τ_{IF} = 50 s, Δ = 25 s and τ_{EF} = 100 s.

3.1.4 M. Bendayan

M. Bendayan and A. Garcia describe a different model in [29], where the chaff cloud is represented by a smaller number of point reflectors, called virtual scatterers. These virtual scatterers are assumed to be uniformly distributed in the cloud and are characterised by their RCS, positions and velocities. The RCS of a single scatterer is given by the total RCS of the cloud divided by the number of virtual scatterers. The cloud centre is updated based on the wind velocity and the chaff fall velocity, while the radius $R_C(t)$ of the cloud is assumed to increase exponentially to a maximum value during the blooming phase, and then remain constant,

$$R_C(t) = \begin{cases} R_{\max} \cdot (1 - e^{\frac{t-t_B}{\tau}}), & t < t_{\max} \\ R_{max}, & t \geq t_{\max}, \end{cases} \tag{3.4}$$

where

$R_{\max}$ = the maximum radius of the cloud [m]
t_B = chaff rocket explosion time [s]
τ = time constant for the blooming cloud (usually a few seconds) [s]
$t_{\max}$ = cloud maximum radius time [s].

The motion of each virtual scatterer consists of two parts, a deterministic one and a random one. During the deterministic part, the position of each scatterer is updated to evenly fill the cloud. During the random part, each scatterer is assigned a normally distributed random velocity to simulate turbulent motion.

The chaff cloud signal is then simulated as the sum of the echoes from each virtual scatterer, given individually as point targets similar to (2.6). In the report, it is shown that with as few as seven virtual scatterers, the power of the generated signal is exponentially distributed, similar to the Swerling 1 model described in section 2.2.1.

3.2 Wing-tip Vortices

The process of wing-tip vortices has been described by the U.S. Department of Transportation in [30] and for NASA by Jim Chow et al. in [31]. The former report focuses mainly on describing the effects in the far-field and the latter in the near-field. The far-field of a vortex system is the area where the vortices have rolled up and started to decay. The near-field describes the process just behind the wings, before the vortices have rolled-up, as seen in figure 2.7. Both reports mention the difficulties with properly describing the processes in detail, and contain several assumptions and simplifications.

3.2.1 Near-Field Vortex Behaviour

Jim Chow et al. have conducted measurements on turbulence in the near-field in [31]. They mention the difficulties in properly describing the near-field due to high turbulent flow, as well as due to large gradients occurring near a curved solid body. According to their own literature study, the majority of articles have focused on describing the far-field. Their findings suggest that initial friction between the air and the wing-tip induces crossflow velocities, resulting in an acceleration of the vortex core to 1.77 times the freestream velocity. The experiment was conducted with an angle of attack of 10 degrees, which is a relatively high angle. Since a higher angle of attack results in an increased lift, and therefore greater wake turbulence, the acceleration of the vortex core increases with increased angle of attack and lift. Furthermore, viscosity seems to play a small role in the velocity of the core. The chaotic nature and large velocities of the near-field vortices make them difficult to simulate. The radius of the core was estimated to be 2-4 cm. This small size made it difficult to use probes to investigate the vortex structures.

Even though simulating the near-field is difficult due to its turbulent nature, some modelling approaches do exist. Mengda Lin et al. describe one such method in [32]. Instead of just modelling two vortices in the far-field, the roll-up phase is also taken into consideration using Large eddy simulation. The model is divided into two parts, a vortex sheet from the trailing edge of the wing and an axial movement from the flight drag. The results were compared with a model only modelling counter-rotating cylindrical vortices. The new model appeared to agree better with recorded data. Furthermore, the results suggest that the roll-up phase plays an important role in far-field decay, so it should be taken into consideration when modelling.

3.2.2 Far-Field Vortex Behaviour and Transport

The US Department of Transportation describes the vortex transport process in [30]. After the vortices have rolled up into two large vortices, they start to descend and move out of the flight corridor, either due to wind effects or by eventually interacting with the ground. Moreover, the vortices age and break up due to viscous decay. The decay is very slow initially, but accelerates after 30-60 seconds.

Depending on the behaviour of the airplane producing vortices, the vortices may behave differently from each other. The effect from wind shear on the vortices is not completely understood, as it varies on multiple variables and is difficult to

compute properly. In certain instances, one of the vortices may tilt differently than the other, causing them to propagate towards the ground with different velocities. One vortex may also decay faster than the other, resulting in just one vortex remaining for a considerably longer time. Wind may cause the vortices to shift sideways relative to the airplane, drifting them to a certain direction, see figure 3.2. This process is not entirely understood either.

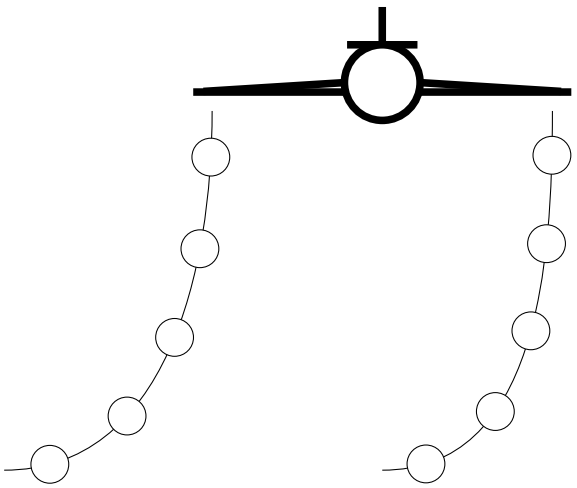

Figure 3.2: Wake vortices may travel both horizontally and vertically.

The rate of decay depends on several factors, such as the weight, speed and wing configuration of the airplane. The wind velocity also contributes to the decaying process. Light winds delay decay, while strong winds will advance decay.

3.3 Aerodynamics Combined with Chaff Clouds

Only a few instances where airplane aerodynamics was combined with chaff were found. Tomasz Jasinski and Mark Cooke have implemented a chaff model combined with aerodynamics in TRIREME [33]. TRIREME is a simulation environment in Simulink for military engagement models. TRIREME does not seem to be available to the public, so using it has not been possible for this thesis. Furthermore, the article explaining the work is simply a presentation and does not give a deep insight into the work process. However, it seems to be based on theories similar to those in section 2.2.2, where the chaff probability density is described by a convection-diffusion equation as in (2.12), with the solution (2.13).

The authors also propose using a Lamb-Oseen vortex for describing the vortex caused by the airplane. It models a vortex decaying by viscosity, and is defined as,

$$V_\theta(r,t) = \frac{\Gamma}{2\pi r}\left(-\exp\left(-\frac{r^2}{r_c^2(t)}\right)\right), \tag{3.5}$$

where

Γ = circulation in the vortex [m^2/s]
r = radius [m]
$r_c(t) = \sqrt{4\nu t + r_c(0)^2}$ is the core radius [m]
ν = kinematic viscosity [m^2/s]
$r_c(0)$ = initial core radius [m].

The TRIREME approach had not been tested with trial data, as this was proposed for future work. It is therefore not known how well this approach actually works.

3.3.1 Previous Work at SAAB

Some work on the subject of wake turbulence and chaff dispersion has already been conducted at SAAB. Y. C-J. Sedin et al. have simulated how an airplane is affected by the vortex wake behind an airplane in the far-field with encouraging results [34]. This report also used (3.5) with some modifications. Compared to flight tests, the dynamic response of the airplane in the simulation was found to be realistic.

A. Näsvall has investigated the distribution of chaff and evolution of RCS in the blooming phase in [35]. According to A. Näsvall, the vortices in the near-field contribute to the dispersion during the blooming phase [15]. In [35], the aerodynamics were modelled with vortices both from an airplane and chaff distributors. Chaff distributors are located close to where the chaff cartridges are emptied and give the chaff an initial spread by concentrating air flow. These distributors help push the chaff into the vortices.

The circulation from the vortices of the distributors are modelled as,

$$\Gamma = \frac{V \cdot c \cdot C_{\mathrm{L}}}{4}, \tag{3.6}$$

$$C_{\mathrm{L}} = \frac{2 \cdot AE \cdot \alpha}{2 + AE}, \tag{3.7}$$

where
V = speed of the airplane [m/s]
c = root chord [m]
AE = aspect ratio [-]
α = angle of attack [deg].

If the lift L of the airplane is known, the circulation from the wing-tip vortices is calculated as,

$$\Gamma = \frac{L}{\rho a V}, \tag{3.8}$$

where
ρ = air density [kg/m^3]
a = wingspan [m]
V = speed of the airplane [m/s].

The velocity vector field behind the airplane is a result of different V velocities at different $\hat{z}$ coordinates,

$$V = \frac{1}{2\pi} \sum_{j=1}^{N} \frac{\Gamma_j}{\hat{z} - \hat{z}_j}, \tag{3.9}$$

where
N = number of vortices [-]
$\hat{z}_j$ = position of vortex j [m].

To simulate a 2D plane the velocities are modelled in the complex plane. The vortices from the distributors are combined with the vortices from the wing-tips. The starting positions and strengths of the vortices depend on the airplane speed and geometry of the distributors. The chaff are modelled as spherical particles with equal speed of descent. The chaff positions as a function of time are calculated using numerical integration.

The calculations are conducted in two steps. Initially, the vortex trajectories are calculated as a function of time. They can be altered to describe the distribution from different starting positions. They are then stored in a matrix and used as input to calculate the trajectories of the chaff using numerical integration. The result is finally stored in vectors. All the calculations at a certain time are in the same geometric plane as the flight direction. Since the positions of the vortices are stored in a matrix, it is possible to calculate the chaff trajectories even if the chaff are not in the same plane. If the chaff are in-between two planes, interpolation is used.

This model is hence completely deterministic. Changing the speed of descent for different chaff create a simulated dispersion. The initial conditions are important for the total of six chaff the model is able to simulate. The RCS is calculated as the area spanned by the chaff positions as viewed by the radar. A complete description, with FORTRAN code and results, can be found in [35].

3.3.2 Video Generator

SAAB has previously developed software capable of simulating radar echoes from one or more airplanes, commonly referred to as targets. This data is used to test signal processing algorithms. The software is based on the theory described in section 2.1.1, with point targets representing airplanes, but also contains more advanced concepts including pulse modulation and some signal processing. With the software, it is possible to define a large range of parameters, for example simulation time, radar PRF, target RCS and flight scenarios. The flight scenarios define a flight path for the radar recording the targets, which is attached to an airplane, and for the targets themselves. The outputs of the simulation are radar signal data which can be plotted in range-Doppler plots, as seen in figure 2.3.

Chapter 4
Modelling

Based on the information provided in the literature study, two models were created. As the thesis is a pilot study, a choice was made to start as simple as possible. Some promising work where chaff were combined with wing-tip vortices had already been conducted by A. Näsvall [35]. The first model, the individual chaff model, was therefore heavily based on this work. It uses the same modelling approach for the wing-tip vortices as well as for the drag effect on chaff in the flight direction. More advanced aerodynamic approaches, also described in the literature study, were not used. The individual chaff model thus attempts to physically simulate the wing-tip vortices created by the airplane and how they affect chaff.

The second model, the Gaussian model, uses a statistical approach. No physical simulation is attempted. Instead, this model is based on the theory described in section 3.1 and uses trends from the models by Ducata et al. in [27] and U. Kaydok in [28]. The concentration as well as the velocities in the cloud are assumed to be normally distributed with time varying means and standard deviations.

Two models were created to test two different approaches. The individual chaff model investigates the possibility to physically simulate the behaviour of the vortices without any consideration to real data. In contrast, the Gaussian model relies on theories from articles and is more suitable to adapt to real data.

Both models were implemented in the video generator, see section 3.3.2, which allowed the creation of range-Doppler plots from the chaff clouds.

An attempt was also made to create a convection-diffusion model. This model proved to be more computer heavy than the others and was not finished. However, it did show promising initial results. Since one aspect of the thesis was to investigate possible modelling approaches it is described in section 4.4.

4.1 Coordinate System for the Chaff Cloud

The coordinate system used for the chaff are based on the directions of the airplane when the chaff are dropped, see figure 4.1. The chaff coordinate system is created once the first chaff are dropped and remains stationary thereafter. The origin of the cloud is the same as the position of the airplane when it started dropping the chaff. As soon as the first chaff have been dropped, the same origin is used for the entire cloud. The vortices affecting the chaff are modelled in the yz plane behind the airplane. A different coordinate system is used by the radar in the

video generator, so the chaff positions are updated in the two different models, and the coordinates are then transformed to the radar coordinate system.

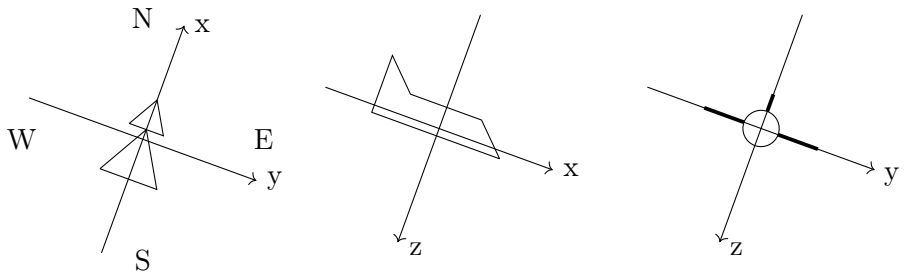

Figure 4.1: Coordinate system used for the target dropping the chaff cloud.

4.2 Individual Chaff Model

The individual chaff model is heavily based on the model described in section 3.3.1. In the model, each chaff is simulated individually and any interaction between the chaff are neglected. The total amount of chaff simulated can be chosen as well as the time-step, allowing for different resolutions. The number of chaff dropped each time-step is then adapted so that all chaff are dropped within 50 ms [36]. A total of two cartridges are emptied, one for each wing-tip, each containing half the total amount of chaff simulated.

4.2.1 Vortex Modelling

The vortices are modelled in the near-field, since these are the vortices which mainly contribute to the blooming phase. Two vortices are modelled in total, one for each wing-tip. The physical representation of the vortices is based on (3.9). To prevent the velocities from diverging to infinity when r reaches 0, they are assumed to be linear within the core. The core radius r_{core} was chosen as 0.05 m since the diameter of a vortex in the near-field is about 0.1 m [15].

One vortex was thus modelled as,

$$\begin{aligned} V_{\text{vortex}}(r) &= \frac{\Gamma}{2\pi r}, \ |r| > r_{\text{core}} \\ V_{\text{vortex}}(r) &= \frac{V_{\text{vortex}}(r_{\text{core}})}{r_{\text{core}}} r, \ |r| \leq r_{\text{core}}, \end{aligned} \tag{4.1}$$

where

Γ = circulation along the wing [m^2/s]
r = radius from centre of vortex core [m]
r_{core} = radius of the vortex core [m].

The circulation Γ was calculated using (3.8) and the lift L using (2.19). Since the lift acts on the entire airplane the value of Γ was divided by the amount of vortices, in this case by two. The distance between the vortices affects the strength of the induced vector field. This distance was set as the wing-span of the airplane. Figure 4.2 shows the velocity as a function of radial distance from the core, and the resulting vortex vector field can be seen in figure 4.3.

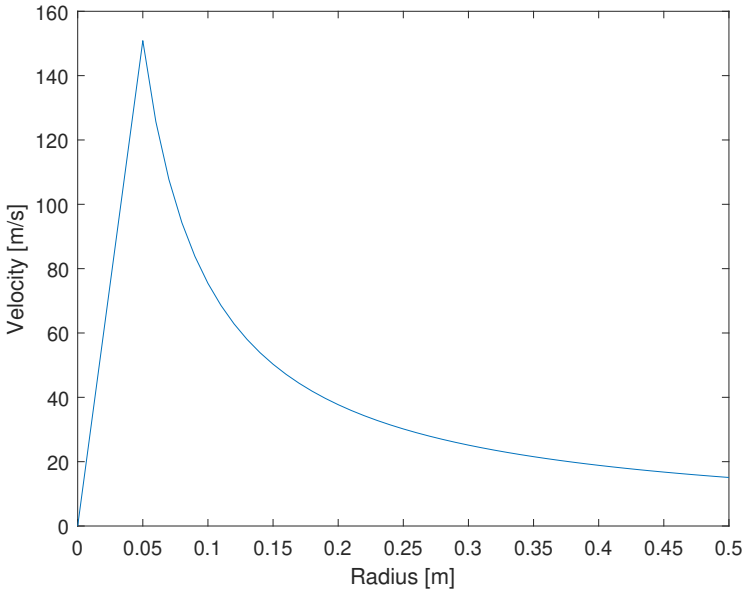

Figure 4.2: Velocity as a function of radial distance from the core.

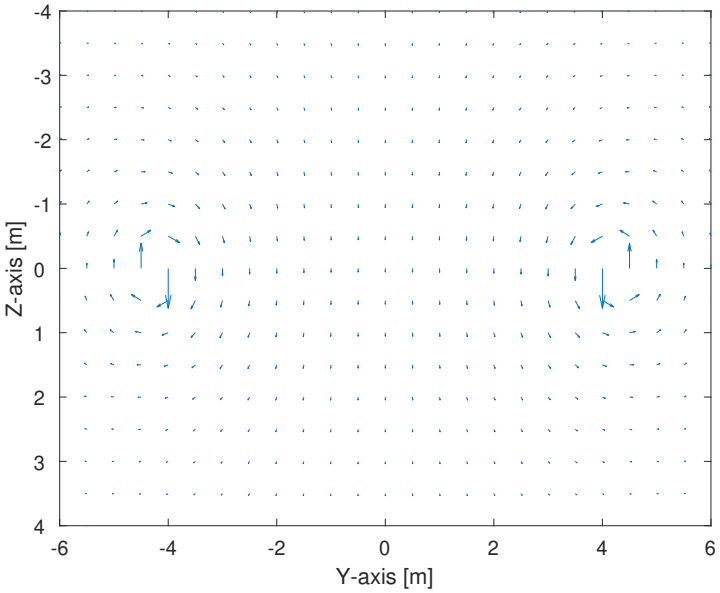

Figure 4.3: Resulting vector field for the two vortices.

4.2.2 Calculating Velocities

The velocities of the chaff perpendicular to the flight direction are directly related to the velocities in the vector field from the vortices. A chaff with position zS and y will have the same velocities U and V as that position in the vector field seen in figure 4.3. In the flight direction, the velocity is initially the same as the airplane and will rapidly decrease due to drag friction with air. It is calculated by substituting F_{D} with $-m\frac{dv}{dt}$ in (2.21),

$$-m\frac{dv}{dt} = \frac{1}{2}\rho v^2 C_{\mathrm{D}} A, \tag{4.2}$$

with the solution,

$$V(t) = \frac{1}{Kt + C}, \tag{4.3}$$

where
K $= \rho C_{\mathrm{D}} A/2m$ [1/m]
C $= 1/V(0)$ is an integration constant [s/m].

The values of m were chosen differently for each chaff from a normal distribution around the mass of one chaff strip. The cross-section A was calculated from a uniform distribution of the total cross-section, the width multiplied with the height of a chaff strip. The trend over how the velocities in the flight direction decrease due to drag friction, i.e. (4.3), where $m = 27.5 \cdot 10^{-9}$ kg and $A = 25 \cdot 10^{-6} \cdot 15 \cdot 10^{-3}$ m^2, can be seen in figure 4.4.

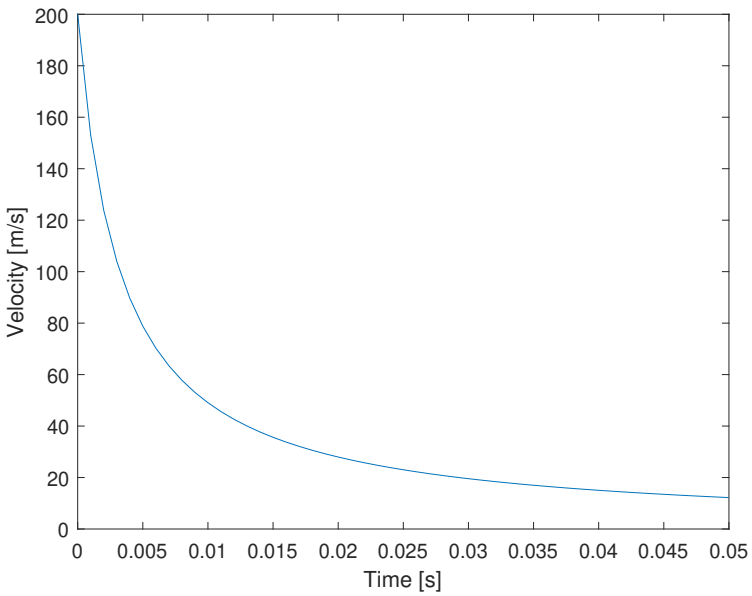

Figure 4.4: Flight direction velocity of a chaff as a function of time. Note that the velocities will be slightly different depending on the m and A values of the individual chaff.

4.2.3 Calculating Positions

The positions were updated by adding the current position with the current velocity multiplied by the simulation time-step. The initial positions in z and y were randomized inside a circle with a diameter of 0.1 m with the dropping point in the centre. The dropping points are the positions of the chaff drop cartridges, one for each wing-tip. They can be changed to investigate the distribution at different positions relative to the wing-tips and the rest of the wing. Instead of simulating the vortices from the distributors, the dropping points were chosen to be very close to the vortex cores. In the flight direction x, the initial positions are updated as the velocity of the airplane times the total time since the start of the simulation, i.e. the current position of the airplane.

The model can thus track the behaviour of chaff affected by wing-tip vortices and friction drag. It is also possible to get the current positions and velocities of each chaff for every time-step. An example plot of a resulting distribution can be seen in figure 4.5.

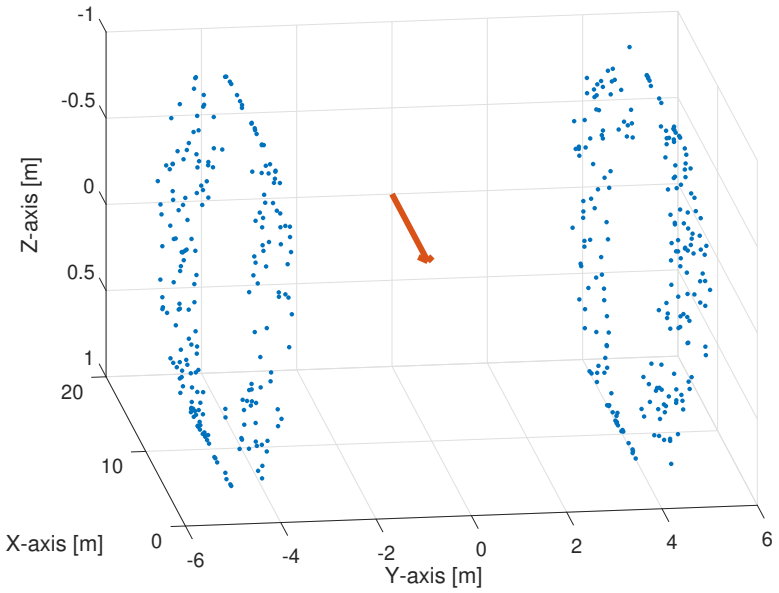

Figure 4.5: Vortex evolution after 10 s. The red arrow indicates the direction of the radar used for calculating RCS.

4.2.4 Calculating RCS

To calculate the RCS, the chaff positions are projected on a 2D plane orthogonal to the radar direction, see figures 4.5, 4.6. The reflectivity and directivity in (2.5) are assumed to be 1, i.e. the RCS is the same as the geometric cross-section. This approach was used in the model proposed by A. Näsvall in [35]. The RCS is calculated as the area enclosed by the boundary points using the built-in MATLAB function boundary(), see figure 4.7. Note that the space between the boundary point is included in the RCS calculation, even though no chaff are present there. This is due to only a few chaff being simulated.

4.2.5 Calculating Radar Signal

The radar signals from the chaff in the cloud are calculated using (2.6). The calculated RCS is divided with the current amount of simulated chaff. The signal is then calculated as the sum of each individual chaff, with different time delays and phases.

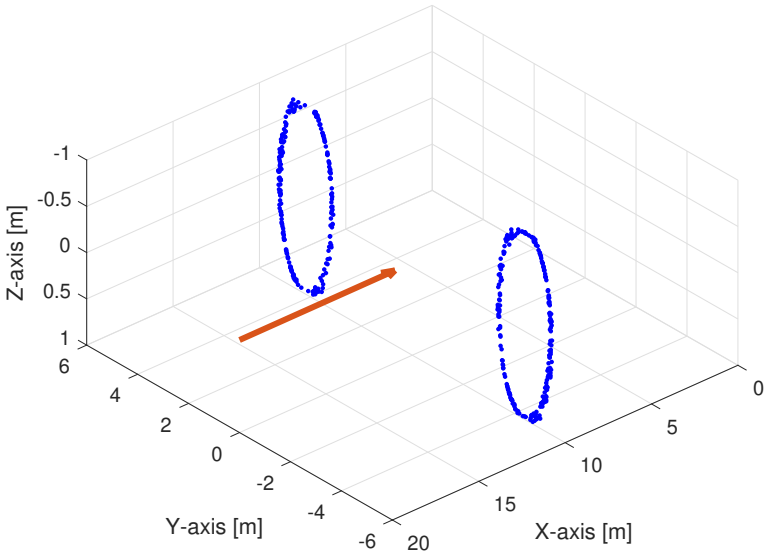

Figure 4.6: 2D plane projected orthogonal to the radar position. The red arrow indicates the direction of the radar.

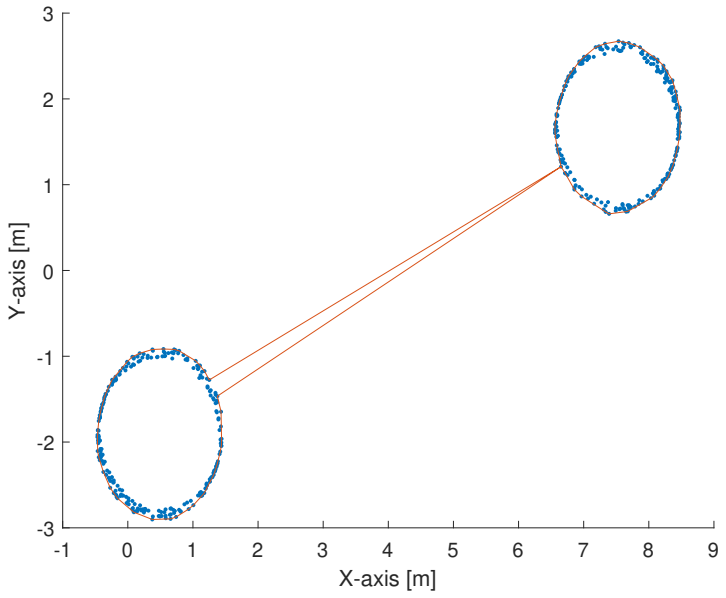

Figure 4.7: RCS calculated from the projection using the MATLAB function boundary().

4.3 Gaussian Model

The philosophy behind the Gaussian model is to have a simple statistical model that is easily adapted to real data or trends based on theory. The positions and velocities in the cloud are represented by different Gaussian distributions. When generating a signal, the velocities and positions for a number of virtual scatterers n_{chaff} are chosen at random from these distributions and the signal is then constructed as the sum of point targets, according to (2.6). It was not possible to use real data due to confidentiality. Instead, this model was adjusted to simulated data from the individual chaff model, during straight flight with 1g.

4.3.1 Calculating Velocities

The velocities of the chaff particles are assumed to be normally distributed around the mean of the cloud centre velocity along each coordinate axis. It is common to assume a normally distributed Doppler spectrum, see section 2.2.3, but the directions of the cloud are rarely taken into consideration. Using separate distributions for each coordinate axis allows the model to simulate the cloud from different aspect angles. The cloud centre velocity is assumed to be equal to the airplane velocity at the dropping time and decrease due to air friction, similar to (4.3). The standard deviations in each direction, $\sigma_{\text{vx}},\ \sigma_{\text{vy}}$, and σ_{vz}, are assumed to be related to the RCS trend (3.2) used in [27] and [28]. Since the simulations in this project focus on the initial phase of the cloud, only the exponential part during the blooming phase is considered,

$$\sigma_{\text{vel}} = -A_1 e^{-A_2 \cdot t} + A_3, \tag{4.4}$$

where
A_1 = adjustable constant [m/s]
A_2 = adjustable constant [1/s]
A_3 = adjustable constant [m/s].

4.3.2 Calculating Positions

Similar to the model by Puolinguen in [26], the chaff probability density at all times is given by a multivariate normal distribution in three dimensions,

$$c(x, y, z) = k e^{-\left[\frac{(x-\mu_x)^2}{2\sigma_x^2} + \frac{(y-\mu_y)^2}{2\sigma_y^2} + \frac{(z-\mu_z)^2}{2\sigma_z^2}\right]}, \tag{4.5}$$

where
k = normalising constant [kg/m^3]
$\mu_x,\ \mu_y,\ \mu_z$ = cloud centre position [m]
$\sigma_x,\ \sigma_y,\ \sigma_z$ = standard deviations along $x,\ y,\ z$ coordinates [m].

The cloud centre position is updated based on the cloud centre velocity. Integrating (4.3) yields,

$$x(t) = \frac{\ln(Kt + C)}{K} + D, \tag{4.6}$$

where
$K = \rho C_{\mathrm{D}} A/2m$ [1/m]
$C = 1/V(0)$ is an integration constant [s/m]
$D = x(0) - \log(C)/K$ is an integration constant [m].

The standard deviations are again given by exponential functions, as in the model proposed by M. Bendayan in [29],

$$\sigma_{\mathrm{pos}} = -B_1 e^{-B_2 \cdot t} + B_3, \tag{4.7}$$

where
B_1 = adjustable constant [m]
B_2 = adjustable constant [1/s]
B_3 = adjustable constant [m].

4.3.3 Calculating RCS

For simplicity, the RCS of the cloud is assumed to be independent of radar recording direction. The RCS is assumed to follow a general form of the trend proposed by U. Kaydok and D. Ducata in [28] and [27],

$$\mathrm{RCS} = -C_1 e^{-C_2 \cdot t} + C_3, \tag{4.8}$$

where
C_1 = adjustable constant [m^2]
C_2 = adjustable constant [1/s]
C_3 = adjustable constant [m^2].

4.3.4 Calculating Radar Signal

The signal is generated as the sum of point target echoes from a number of virtual scatterers, similar to the model described in section 3.1.4. Each echo is calculated using (2.7) and (2.6) in the video generator. The velocities and positions of each scatterer are chosen at random from the distributions described above. New values are chosen at each time step. The RCS of each virtual scatterer is given by the cloud RCS divided by the total number of virtual scatterers n_{chaff}.

4.4 Convection-Diffusion Model

The convection-diffusion model is a numeric model based on the convection-diffusion equation described in (2.14). It models the concentration $p(x, y, z, t)$ of chaff in three dimensions when affected by the vortices. The model uses a symmetric three dimensional Cartesian grid with a uniform grid spacing h and assumes the diffusion coefficients to be the same in all directions, $D = D_x = D_y = D_z$, and constant in time and space. The numerical scheme is described as,

$$\frac{\partial p}{\partial t} = \frac{p(x, y, z, t + \Delta t) - p(x, y, z, t)}{\Delta t} \tag{4.9}$$

$$\frac{\partial p}{\partial x} = \frac{p(x + h, y, z, t) - p(x - h, y, z, t)}{2h} \tag{4.10}$$

$$\frac{\partial^2 p}{\partial x^2} = \frac{p(x + h, y, z, t) - 2p(x, y, z, t) + p(x - h, y, z, t)}{h^2}, \tag{4.11}$$

where
Δt = time step [s]
h = grid spacing [m].

The velocities perpendicular to the flight direction, A_y and A_z, were assumed to be constant along the x-axis and taken from the vortex model in (4.1) and the velocity along the flight direction, A_x, was modelled similar to the individual chaff model using (4.3).

The model calculates the concentration distribution in space at each time step. As previously mentioned, the model was never completed and properly tested as the other models. The main reason was due to it being too computer heavy since it required a small time step and grid spacing for stability. Initial testing of the model did show promising results however and it should be further investigated, especially since it was able to account for diffusion effects which the other models are not.

4.5 Test Scenarios

To evaluate the models, it would be preferable to use real recorded data. However, this was not possible since the data is classified. The individual chaff model was therefore evaluated by simulating two simple flight scenarios. Since the philosophy behind the Gaussian model was to make it adaptable to data, it was adapted to the results from the individual chaff model instead of real data.

4.5.1 Straight-Flight Test

The conditions for the straight-flight test can be seen in figure 4.8. The airplane with the tracking radar has a velocity of 210 m/s along the x-axis. The target airplane, which drops the chaff cloud, has a velocity of -200 m/s along the x-axis. The y and z coordinates for both the radar and the target remain the same.

4.5.2 Zero-Doppler Flight Test

The second scenario can be seen in figure 4.9. The initial conditions are the same as in the straight-flight test. In a zero-Doppler scenario a target will be observed as a stationary target, as it is flying perpendicular to the radar [6, ch. 8.3]. The airplane with the tracking radar has again a velocity of 210 m/s along the x-axis. The target airplane which drops the chaff cloud has a velocity of -200 m/s along the y-axis. The z coordinates for both the radar and the target remain the same.

4.5.3 Cloud Size Evaluation

To evaluate if the model was able to simulate RCS values properly, the simulation was run separately outside of the video generator with a load factor of three to produce the same type of figures as figure 4.5. The width and height were then compared with the values in table 2.1 at the corresponding times.

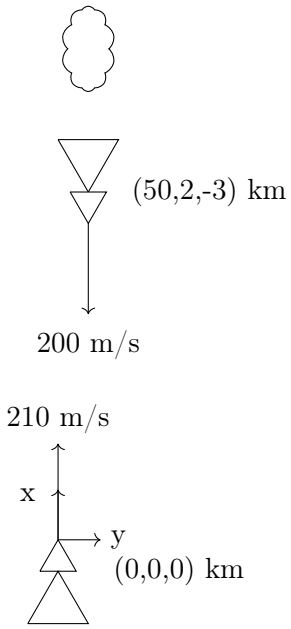

Figure 4.8: Initial conditions for the straight-flight test scenario.

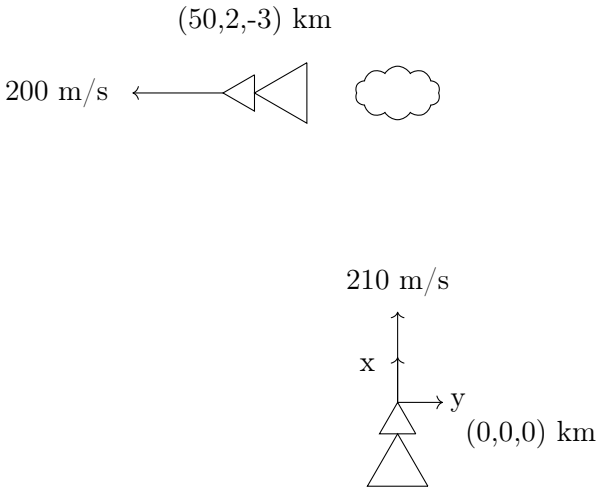

Figure 4.9: Initial conditions for the zero-Doppler flight test scenario.

4.6 Parameters Used for Simulation

4.6.1 Video Generator Settings

The models were implemented in the video generator created at SAAB. The two flight tests were simulated with different setup conditions depending on model. The settings for generating the signals for the two flight tests were:

Setting:	Value:
Number of PRI [-]	116
Target RCS [m^2]	10
PRI duration [s]	$984 \cdot 10^{-7}$
Duty factor [-]	0.1
Noise amplitude [dB]	-50

Table 4.1: Settings for video generator.

4.6.2 Individual Chaff Model Parameters

The following equation parameters were used for the individual chaff model:

Parameter:	Value:
Airplane mass [kg]	6622
ρ_{air} [kg/m^3]	1.225
Wingspan [m]	8.4
Dropping point[1] [m]	± 4.1
r_{core} [m]	0.05
Number of simulated chaff [-]	500
Mean chaff mass [kg]	$27.5 \cdot 10^{-9}$
Mean chaff height [m]	$15 \cdot 10^{-3}$
Chaff width [m]	$25 \cdot 10^{-6}$
Chaff drag coefficient (C_{D}) [-]	0.1503

Table 4.2: Individual chaff model parameters.

The banking angle was changed according (2.20) depending on the load factor used during the specific scenario.

4.6.3 Gaussian Model Parameters

The following physical parameters were used in the Gaussian model:

[1] From airplane centre.

Parameter:	Value:
ρ_{air} [kg/m^3]	1.225
Number of simulated chaff [-]	50
Mean chaff mass [kg]	$27.5 \cdot 10^{-9}$
Mean chaff height [m]	$15 \cdot 10^{-3}$
Chaff width [m]	$25 \cdot 10^{-6}$
Chaff drag coefficient (C_{D}) [-]	0.1503

Table 4.3: Gaussian model parameters.

The parameter values used in (4.4), (4.7) and (4.8) can be seen in table 4.4. They were derived using a curve fitting algorithm in MATLAB. The algorithm minimized the norm of the residual between the function values and the simulated data from the individual chaff model during straight flight, by using the MATLAB function fminsearch(). The simulated data as well as the fitted curves can be seen in appendix A.

Parameter:	Value:
A_{x1}, A_{x2}, A_{x3}	-90.8, 26.4, 0.00809.
A_{y1}, A_{y2}, A_{y3}	-4.53, 1.41, 3.92
A_{z1}, A_{z2}, A_{z3}	-4.53, 1.41, 3.92
B_{x1}, B_{x2}, B_{x3}	3.15, 29.8, 2.91
B_{y1}, B_{y2}, B_{y3}	5.14, 33.0, 4.25
B_{z1}, B_{z2}, B_{z3}	0.193, 0.676, 0.343
C_1, C_2, C_3	4.31, 0.677, 7.87

Table 4.4: Gaussian model trend parameters.

Chapter 5
Results and Discussion

The following section contains the results from the two test scenarios for the individual chaff model. The Gaussian model was adapted to these results, and since its results are very similar to the results from the individual chaff model, they can be seen in appendix A. A major part of the results are range-Doppler plots for different times during the simulation. The range-Doppler plots show the signal power in dB of the echo from the target and the chaff cloud. From these plots, one column of ranges at a specific range-rate in the chaff cloud was chosen. Similarly, one row of range-rates at a specific range was also chosen, as described using red lines in figure 5.1a. These are then plotted to give a better overview of the signal strengths as well as the range and range-rate distributions, see figures 5.1b and 5.1c.

In this example, the range distribution was chosen at range-rate 78.88 m/s, seen in figure 5.1b, and the range-rate distribution was chosen at range 5876 m, seen in figure 5.1c. The red lines in figure 5.1a corresponds to the range column and range-rate row, which were chosen manually as the approximate centre of the cloud in the range-Doppler figures. Their distributions are shown in figure 5.1b and figure 5.1c. The highest peak in figure 5.1c corresponds to the target. The red lines in figure 5.1b and figure 5.1c are arbitrarily chosen thresholds to differentiate noise from the signals.

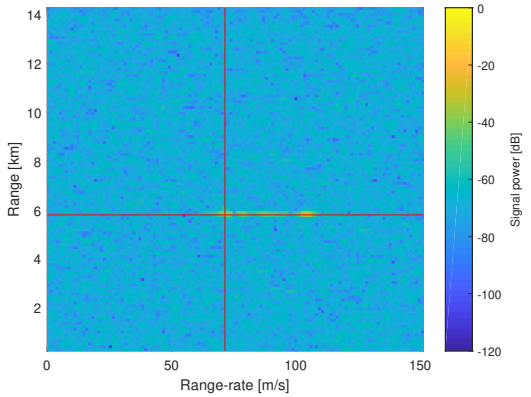

(a) Range-Doppler plot with a specific column and row selected.

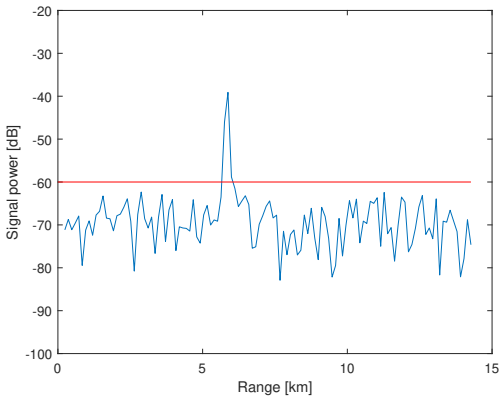

(b) Range distribution at range-rate 78.88 m/s.

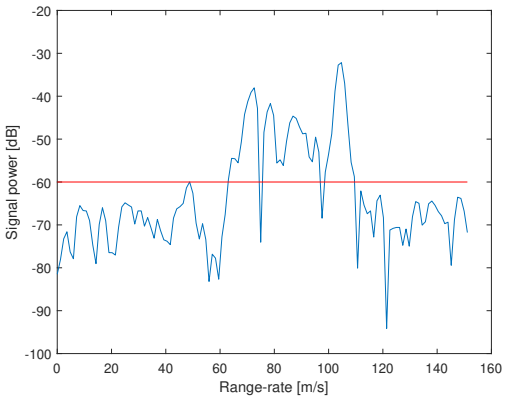

(c) Range-rate distribution at range 5876 m.

Figure 5.1: Method for selecting column and row to analyse range and range-rate distributions.

The same procedure was repeated for the range-Doppler plots in figures 5.2 and 5.9. The range-Doppler figures are shown together for six different times, then the range distributions and finally the velocity distributions. This allows for easier comparison at different times. Note that different ranges and range-rates have been chosen for different figures, to analyse the signal from the chaff cloud at different times. The first range-Doppler plot, 5.2a and 5.9a, are the first figures where any signal can be seen and were chosen 13.2 ms after drop. Figures 5.2b-5.2d and 5.9b-5.9d, were chosen at times when the entire cloud had been dropped, with an interval of roughly 12 ms in-between each figure. Figures 5.2e and 5.9e were chosen about one second after drop. Lastly, figures 5.2f and 5.9f were chosen almost four seconds after drop. The corresponding range and range-rate distributions for the range-Doppler plots can be seen in figures 5.3 and 5.4 for straight flight, and in figures 5.10 and 5.11 for zero-Doppler flight.

5.1 Individual Chaff Model

5.1.1 Straight Flight

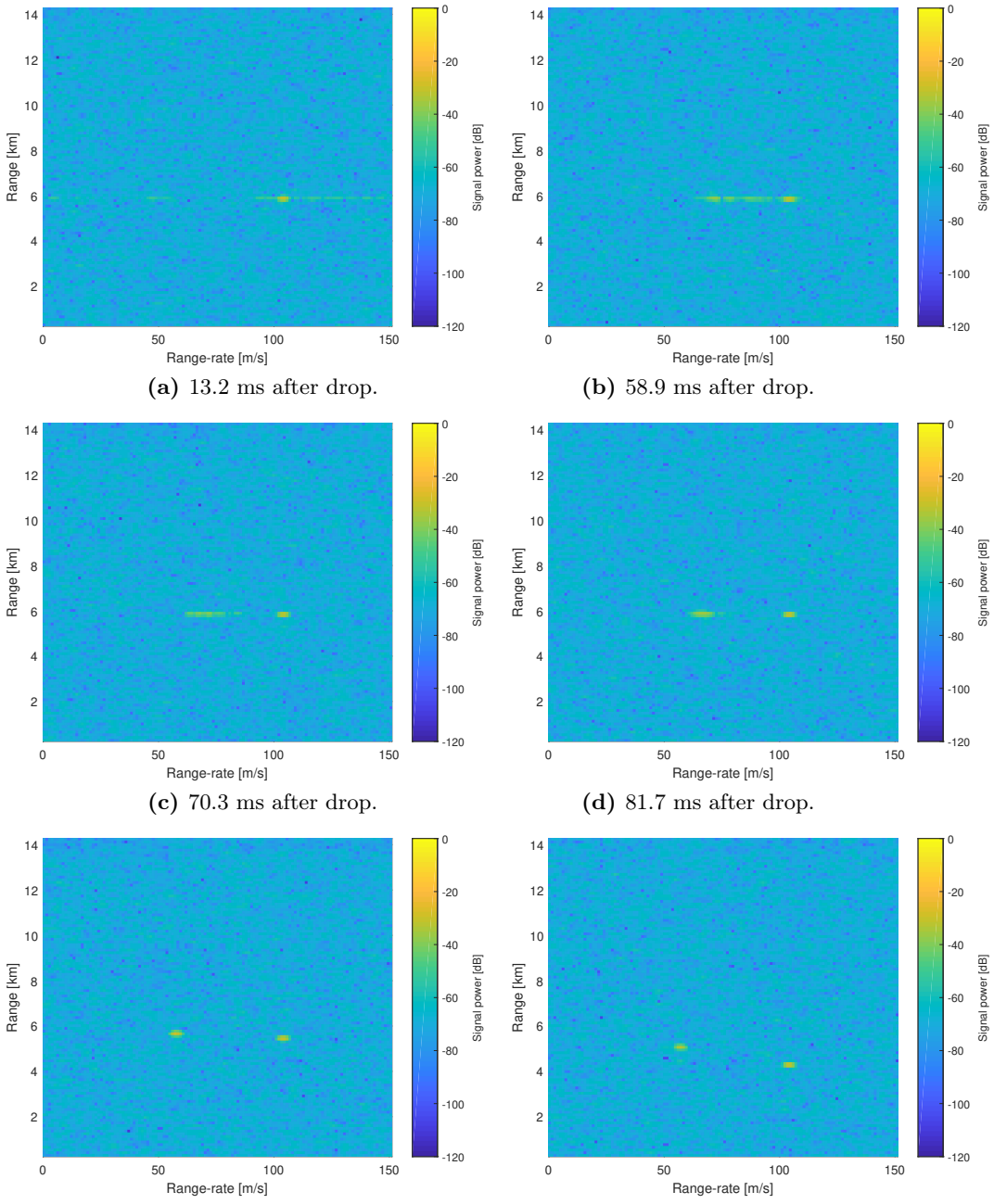

(a) 13.2 ms after drop.

(b) 58.9 ms after drop.

(c) 70.3 ms after drop.

(d) 81.7 ms after drop.

(e) 1017.7 ms after drop.

(f) 3894.1 ms after drop.

Figure 5.2: Range-Doppler spectra at different times.

Range Distributions

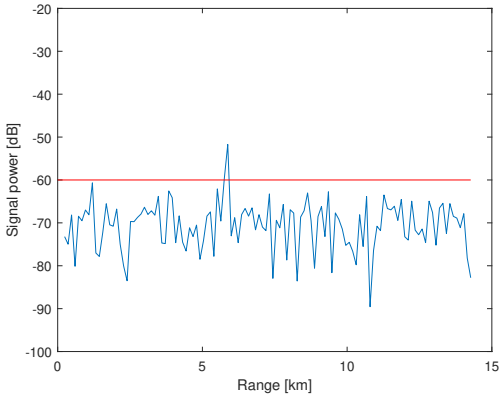

(a) Range distribution at 48.79 m/s, 13.2 ms after drop.

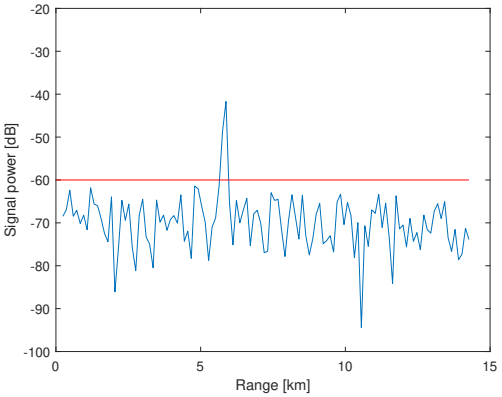

(b) Range distribution at 78.55 m/s, 58.9 ms after drop.

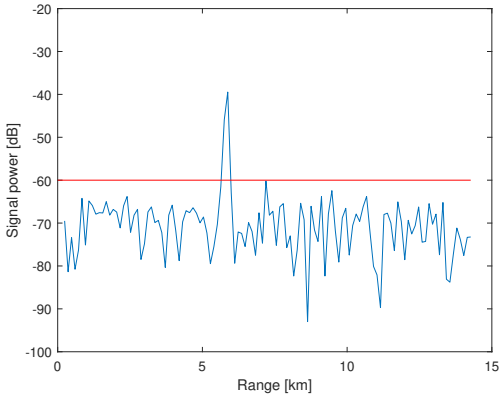

(c) Range distribution at 71.41 m/s, 70.3 ms after drop.

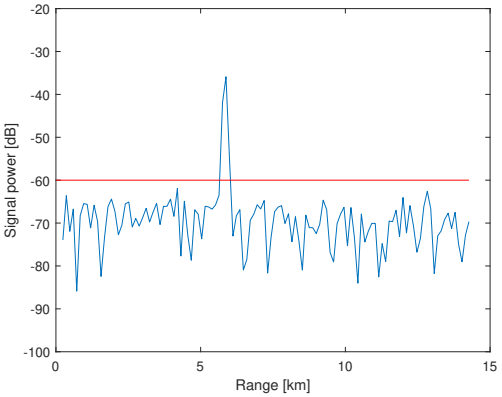

(d) Range distribution at 66.65 m/s, 81.7 ms after drop.

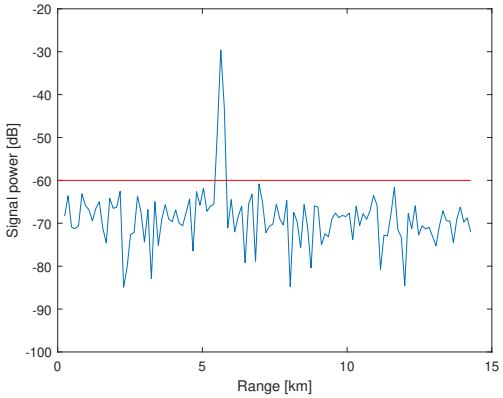

(e) Range distribution at 57.13 m/s, 1017.7 ms after drop.

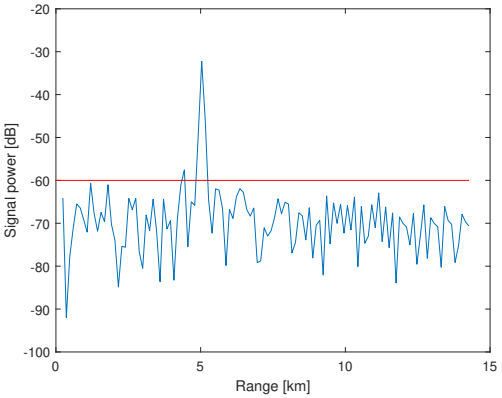

(f) Range distribution at 57.13 m/s, 3894.1 ms after drop.

Figure 5.3: Range distributions at different range-rates and times for straight-flight.

Range-Rate Distributions

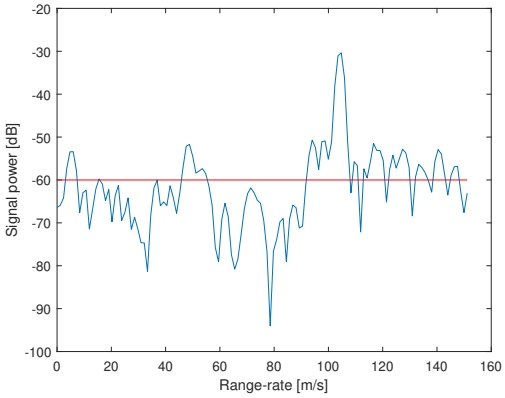

(a) Range-rate distribution at 5876 m, 13.2 ms after drop.

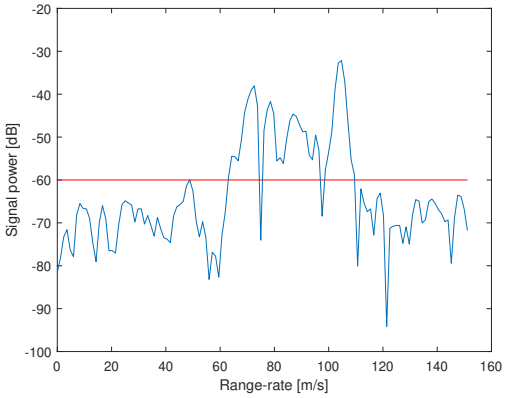

(b) Range-rate distribution at 5876 m, 58.9 ms after drop.

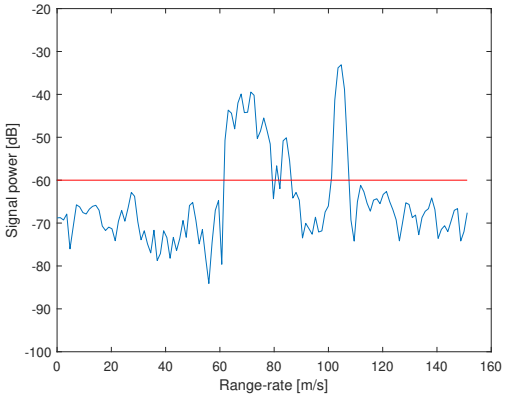

(c) Range-rate distribution at 5876 m, 70.3 ms after drop.

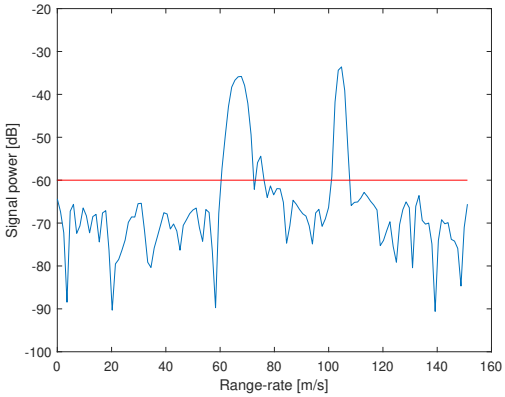

(d) Range-rate distribution at 5876 m, 81.7 ms after drop.

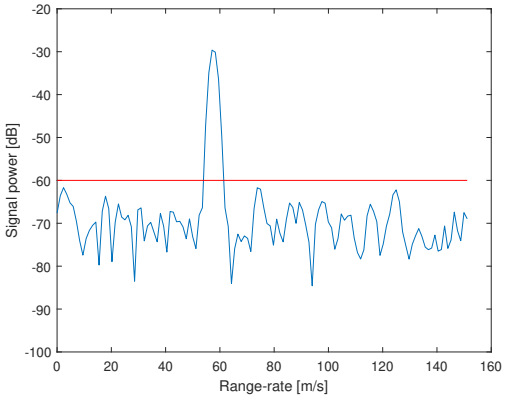

(e) Range-rate distribution at 5636 m, 1017.7 ms after drop.

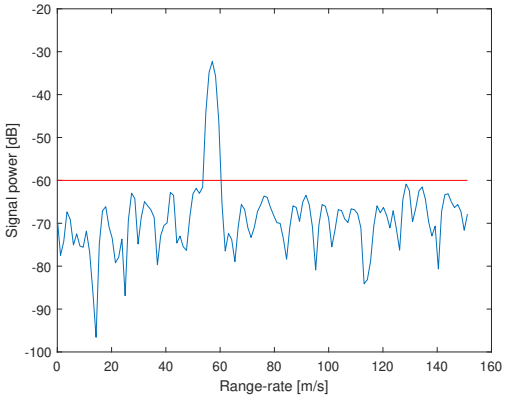

(f) Range-rate distribution at 5037 m, 3894.1 ms after drop.

Figure 5.4: Velocity distributions at different ranges and times for straight-flight.

In the range-Doppler and range-rate distribution figures, the range-rates are relative to the radar. A stationary object relative to the ground would have a range-rate of 210 m/s which is the same as the velocity of the radar, and is shown as roughly 50 m/s in these figures due to folding, see section 2.1.1. Similarly, since the maximum unambiguous range of the radar is 14 km, the ranges of the target and the chaff cloud are ambiguous and appear at lower values. Figure 5.2a is the first range-Doppler plot where a signal from the cloud can be seen. Although the signal strength is low, the figure indicates a large spread in range-rate. Since not all chaff have been simulated yet, and due to the large spread, the result is a low signal strength. This behaviour can also be seen in the corresponding range-rate distribution seen in figure 5.4a. Due to the low signal strength most of the signal is beneath the noise level. Note that the peak in this figure is the peak from the target.

In comparison, figure 5.2b shows a higher signal strength. In this figure 58.9 ms have passed since drop which means all simulated chaff have been dropped, as they are dropped within 50 ms. Since more time has passed, the spread is lower and more chaff are simulated, resulting in a higher signal strength. Figures 5.2c and 5.2d show the succeeding times, and the spread is reduced further, indicating a rapidly decreasing range-rate spread. The same phenomena for all three figures can also be seen in their corresponding range-rate distribution figures, 5.4b, 5.4c and 5.4d, respectively. It can be seen that the range-rate of the chaff cloud converges to 53.4 m/s, which is close to 0 m/s relative to the ground. The range distributions in figure 5.3 show an increase in signal strength over time as well as gradually lower range values. This is due to the fact that the radar moves closer to the cloud, which results in an overall stronger signal.

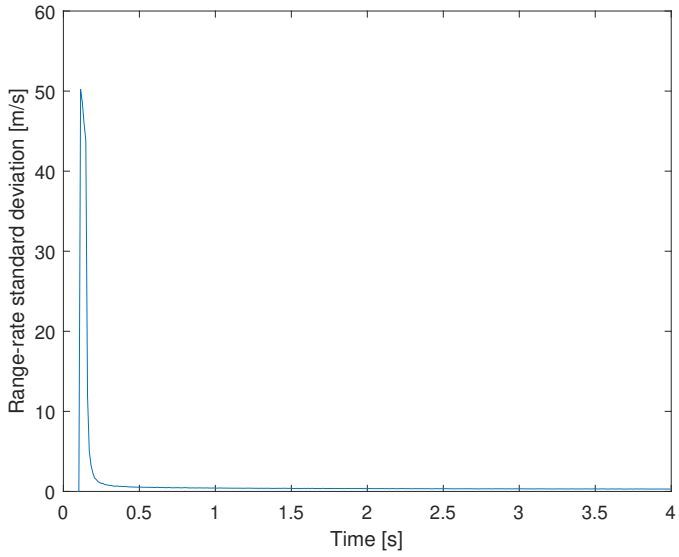

Figure 5.5: Standard deviation of range-rates at different times for straight-flight.

Figure 5.5 shows how the standard deviation of the range-rate of the chaff cloud changes with time. The initial peak at 0.1 s indicates the moment the chaff cloud was dropped. The figure shows a similar trend as the range-Doppler and range-rate figures above. At first, the range-rate has a large spread which quickly decreases due to drag friction with air. However, it is not reasonable that the range-rates converges this quickly to 0. In reality, atmospheric turbulence and local winds will affect the chaff when the dropping airplane has left the area, see section 2.2.3.

RCS Evaluation

Figure 5.6 shows the mean RCS of the chaff cloud in straight-flight as a function of time. The RCS follows a similar exponential trend as the first part of (3.2), shown in figure 3.1. Due to the small simulation time, the cloud never reaches the mature phase. The RCS converges towards a value of approximately 8 m^2. It can be compared to (2.8) and (2.9). A cloud of 10^6 chaff in which 50% are operational and with a radar wavelength of 0.03 m would give a RCS value of 38.25 m^2. Thus, the model is not able to simulate accurate RCS values. This is most likely due to an insufficient diffusion simulation.

Figure 5.7 shows the effective RCS values recorded by the radar in straight-flight. The same values in a histogram can be seen in figure 5.8. The red line in the histogram shows a probability density function of an exponential distribution fitted to the data. Thus the data seems to correspond with a Swerling model since it follows an exponential distribution, as explained in 2.2.1.

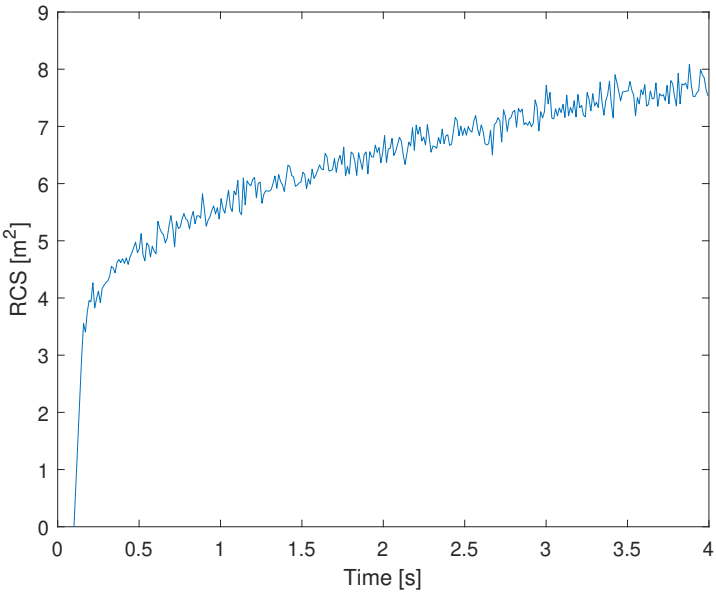

Figure 5.6: Mean RCS as a function of time.

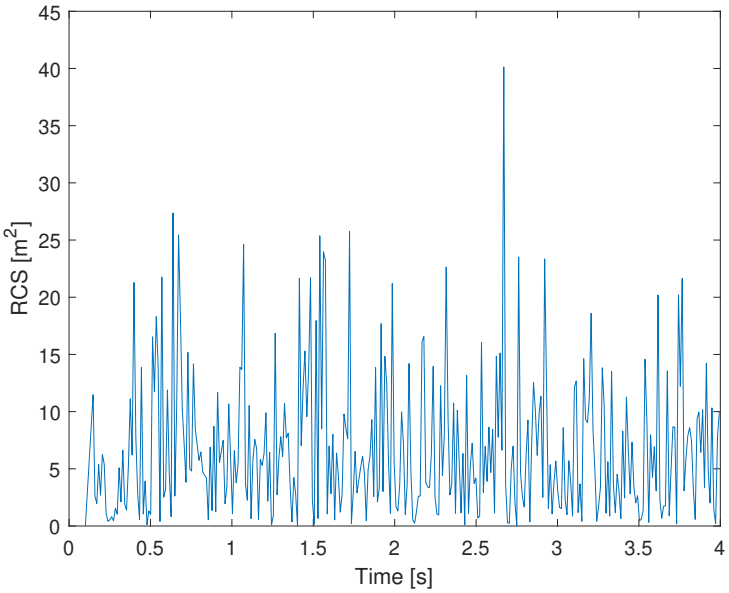

Figure 5.7: Effective RCS as a function of time.

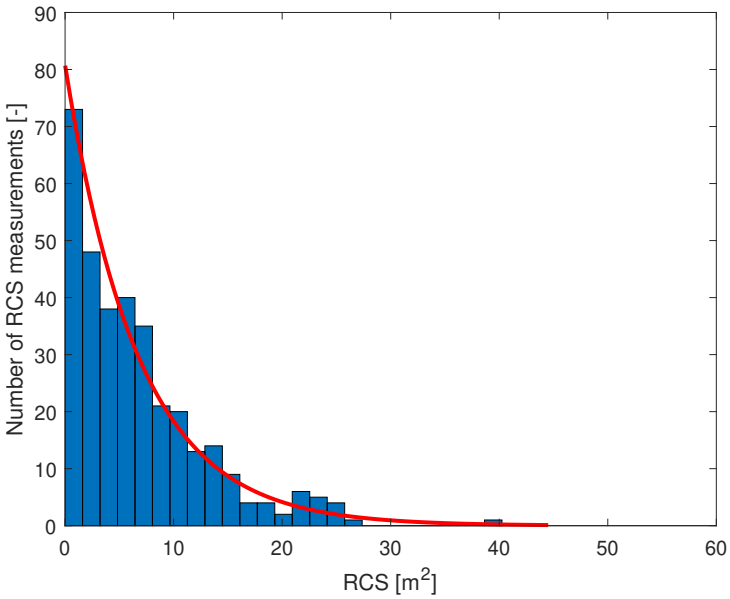

Figure 5.8: Histogram of effective RCS values.

5.1.2 Zero-Doppler Flight

Range-Doppler Plots

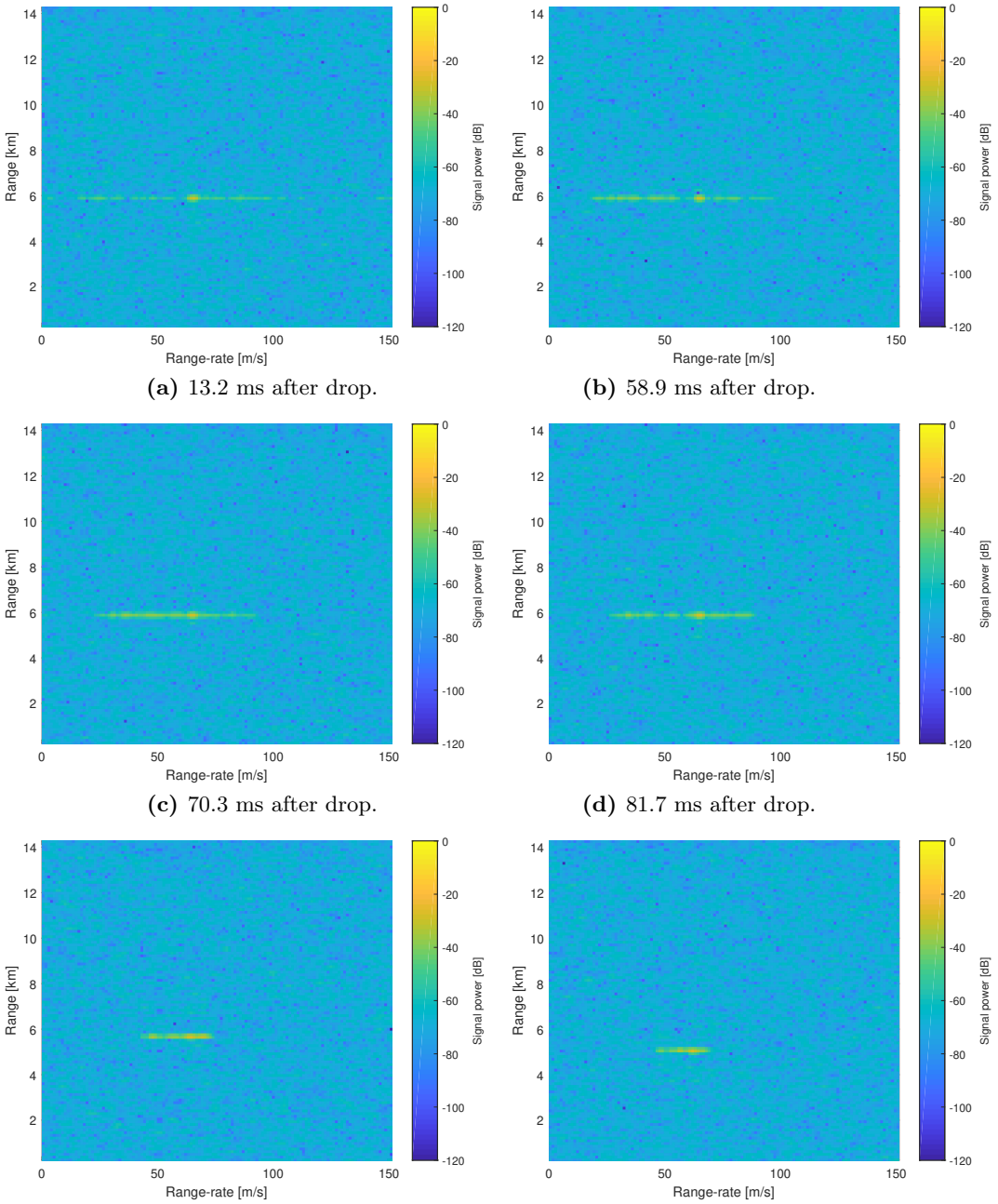

(a) 13.2 ms after drop.

(b) 58.9 ms after drop.

(c) 70.3 ms after drop.

(d) 81.7 ms after drop.

(e) 1017.7 ms after drop.

(f) 3894.1 ms after drop.

Figure 5.9: Range-Doppler spectra from zero-Doppler flight at different times.

Range Distributions

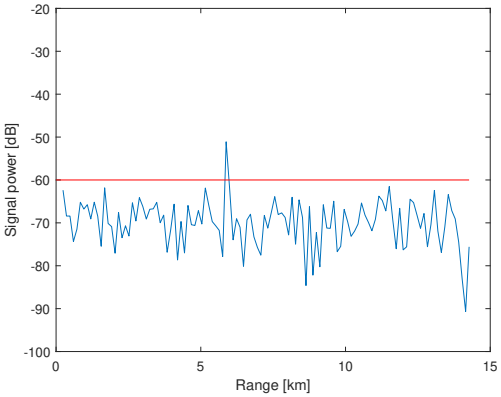

(a) Range distribution at 47.6 m/s, 13.2 ms after drop.

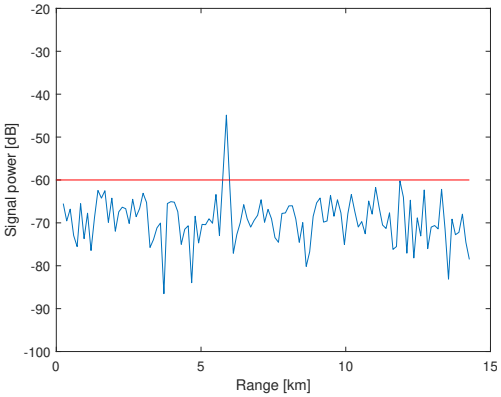

(b) Range distribution at 47.6 m/s, 58.9 ms after drop.

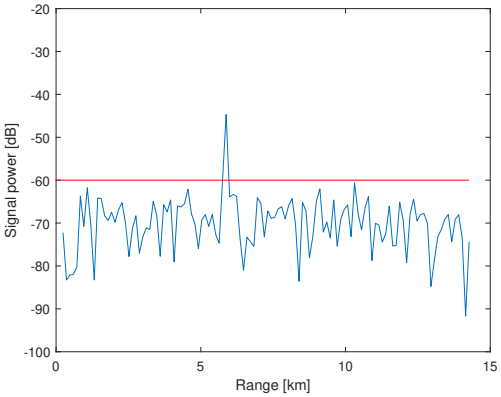

(c) Range distribution at 49.98 m/s, 70.3 ms after drop.

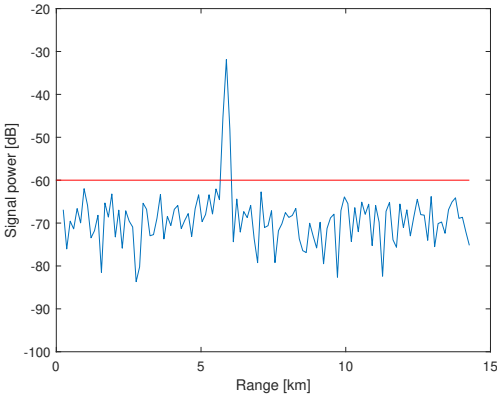

(d) Range distribution at 44.03 m/s, 81.7 ms after drop.

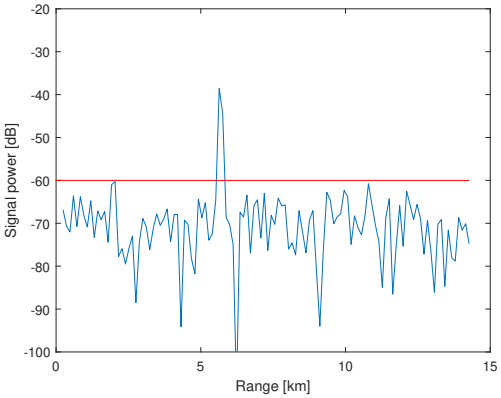

(e) Range distribution at 58.32 m/s, 1017.7 ms after drop.

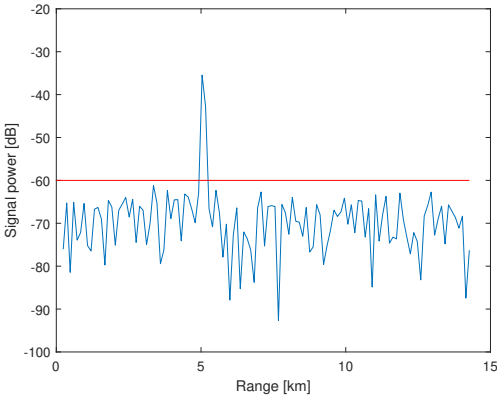

(f) Range distribution at 55.93 m/s 3894.1 ms after drop.

Figure 5.10: Range distributions at different range-rates and times for zero-Doppler flight.

Range-Rate Distributions

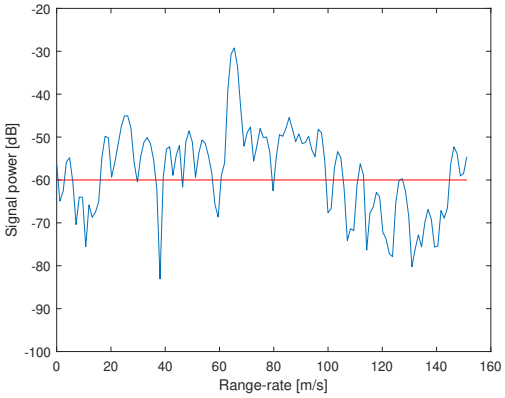

(a) Range-rate distribution at 5876 m, 13.2 ms after drop.

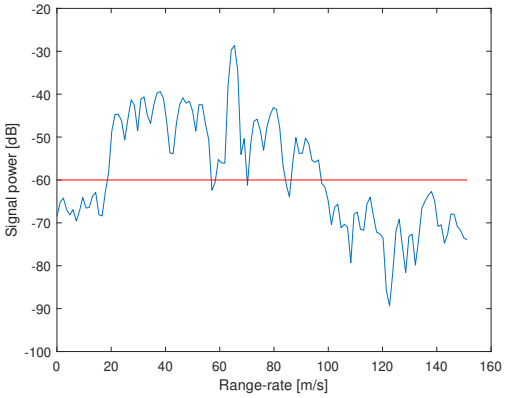

(b) Range-rate distribution at 5876 m, 58.9 ms after drop.

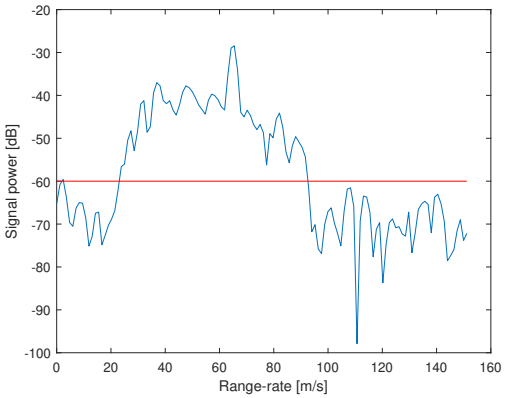

(c) Range-rate distribution at 5876 m, 70.3 ms after drop.

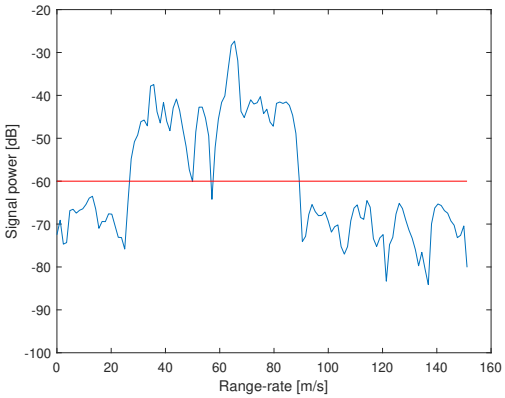

(d) Range-rate distribution at 5876 m, 81.7 ms after drop.

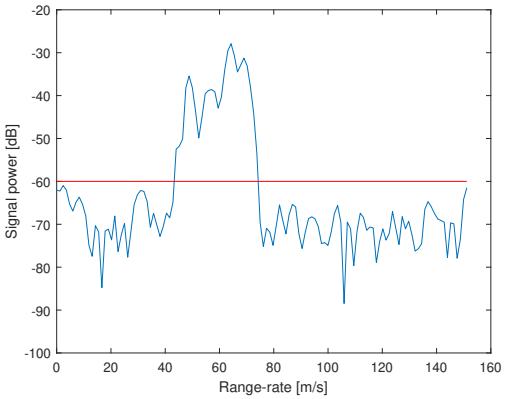

(e) Range-rate distribution at 5636 m, 1017.7 ms after drop.

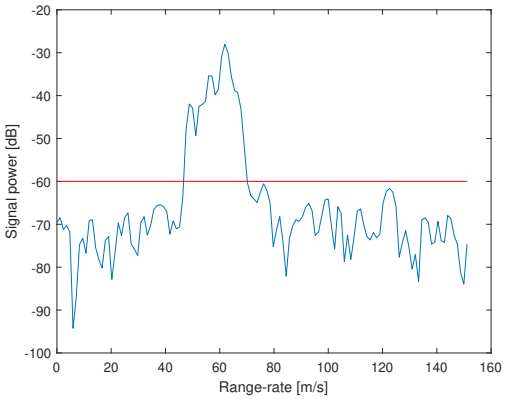

(f) Range-rate distribution at 5037 m 3894.1 ms after drop.

Figure 5.11: Velocity distributions at different ranges and times for zero-Doppler flight.

Figure 5.9a shows a higher signal strength value if compared to 5.2a, even though the same amount of chaff are simulated. This is a result of a lower spread in range-rate for the zero-Doppler case, which also can be seen in the figure 5.11a. Figures 5.9b, 5.9c and 5.9d show a high initial spread in range-rate. Compared to the straight-flight scenario, the range-rate spread remains for a longer period of time, even after one second since drop as seen in figures 5.9e and 5.11e. This is a result of the chaff still being affected by the vortices which is recorded by the radar since it is perpendicular to the cloud. The same behaviour can be seen in the range-rate distributions in figure 5.11. Observing the range distributions in figure 5.10, it can again be seen that the signal strengths increase and that the range values decrease. Just as for the straight-flight scenario, this is a result of the radar moving closer to the chaff cloud.

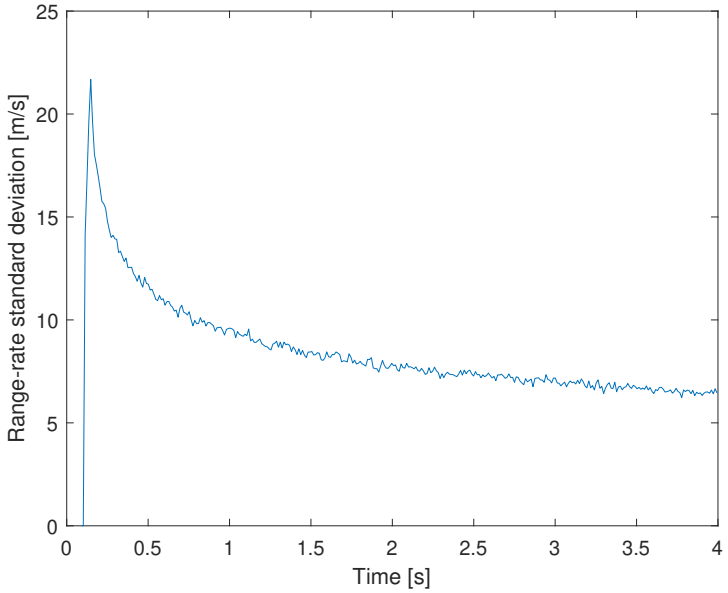

Figure 5.12: Standard deviation of range-rates at different times for zero-Doppler flight.

Figure 5.12 shows how the range-rate spread of the chaff cloud changes over time. Just as in figure 5.5, the range-rate increases rapidly when the cloud is dropped. The peak is not as large since the velocities from the vortices are lower than the velocity of the target airplane. Furthermore, the range-rates do not decrease as quickly or converge to 0. Instead, the range-rate converges to around 7 m/s. This indicates that the chaff remain within the vortices well after drop.

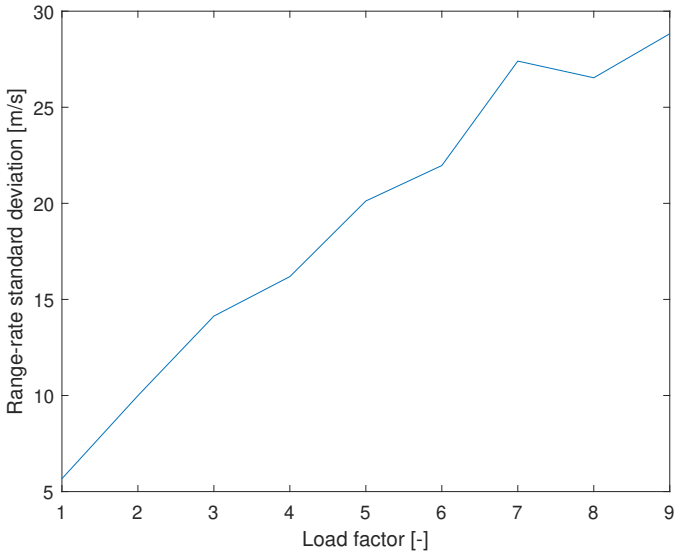

Figure 5.13: Standard deviations of range-rates at 13.2 ms after drop for different load factors.

Figure 5.13 shows how the initial range-rate spread increases with the load factor. The figure indicates that the larger g-force the airplane is exposed to, the higher the standard deviation of the range-rate will be when the cloud is dropped. This is reasonable since it is known from the literature study that a higher load on the airplane will result in stronger wing-tip vortices.

RCS Evaluation

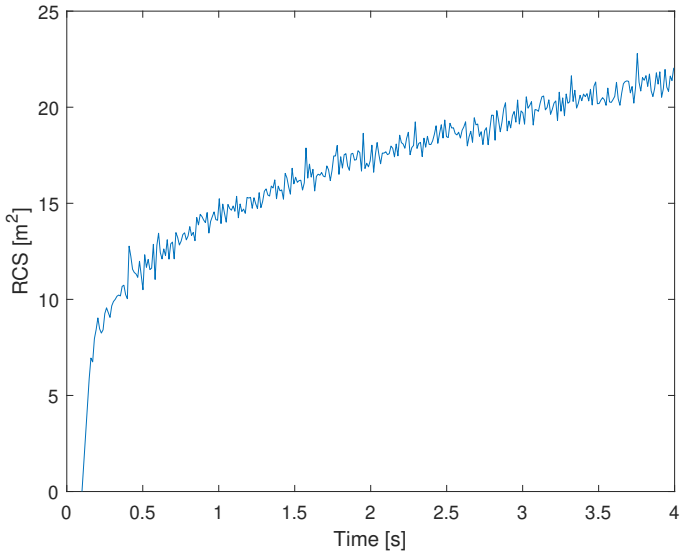

Figure 5.14: Mean RCS as a function of time.

Figure 5.14 shows, just as figure 5.6, the mean of the RCS over time, but now for the zero-Doppler flight. Again, the trend of the RCS corresponds with (3.2) and figure 3.1, and does not converge to a realistic value. The value is still a bit better than the straight flight scenario.

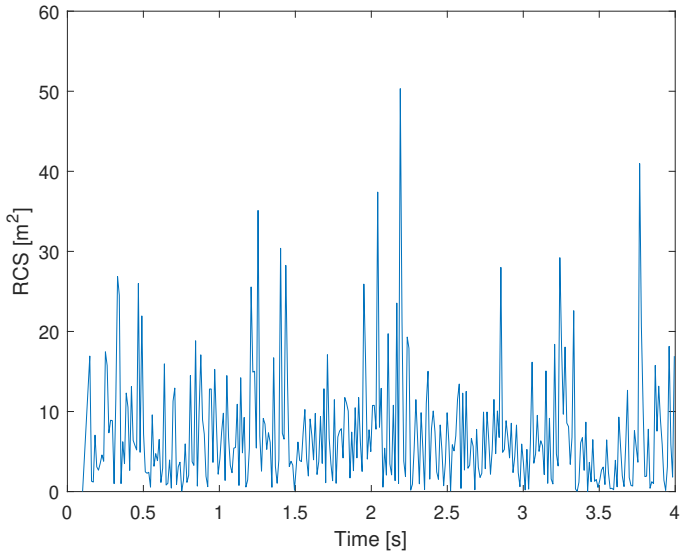

Figure 5.15: Effective RCS as a function of time.

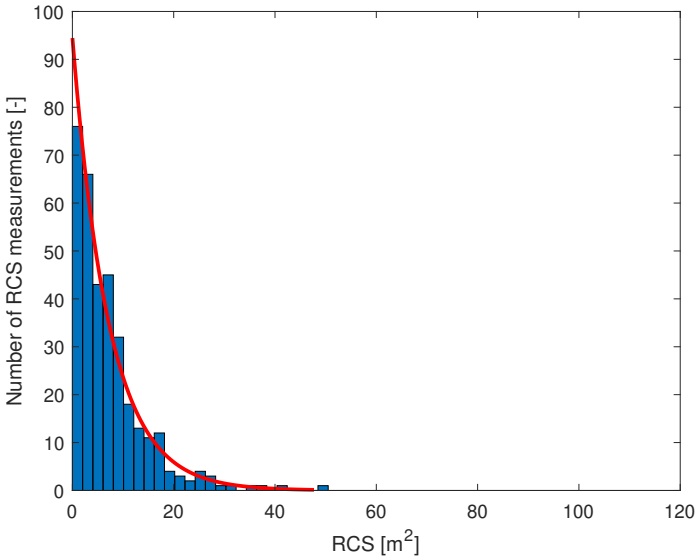

Figure 5.16: Histogram of effective RCS values.

Figures 5.15 and 5.16 show, just as figures 5.7 and 5.8, that the data again is exponentially distributed, similar to a Swerling model.

Time	Width	Height
50 ms	1.942 m	0.6747 m
100 ms	5.219 m	0.6541 m
60 s	6.627 m	3.266 m

Table 5.1: Chaff cloud sizes at specific times after drop for zero-Doppler flight.

The size of the chaff cloud at different times for the zero-Doppler scenario can be seen in table 5.1. Note that these values are taken from each individual cylinder. Comparing these to table 2.1, it can be seen that the size of the simulated chaff cloud does not correspond with real values, especially after a long time. This is due to the fact that the diffusion has not been properly simulated, even though the dropping point was set close to the vortex cores. The chaff do not disperse properly but remain within the vortex trajectories, see figure 5.17. Since the chaff remain in the cylinders and do not create a cloud it is not possible to perform a proper comparison. Moreover, as mentioned in section 4.2.4, there are no chaff present in-between the boundary points. This is a result of only a few chaff being simulated but also due to insufficient diffusion simulation. In reality, there would be chaff present inside both cylinders, which is why the entirety of the cross-section is used to calculate the RCS, as seen in figure 4.7.

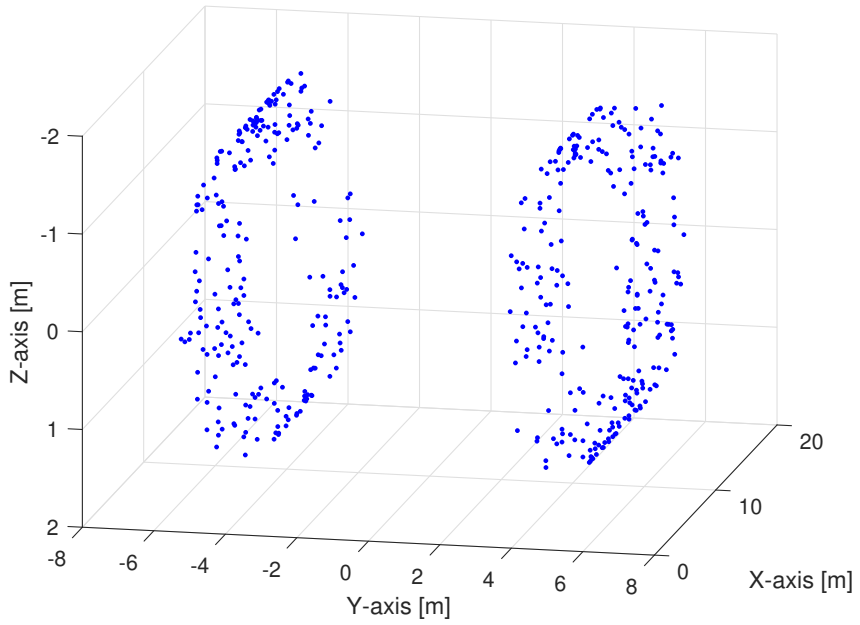

Figure 5.17: Chaff distribution after 60 s at zero-Doppler flight.

5.1.3 General Discussion

Comparing the figures from the straight-flight scenario with the zero-Doppler scenario, both flight scenarios result in a high initial spread in range-rate. For the straight flight, this is due to the fact that the chaff velocities are the same as for the airplane when dropped and then rapidly decrease due to drag friction with air. Since the chaff are dropped during a period of 50 ms, and have different masses and cross-sectional areas, they will have different velocities, resulting in a spread in range-rate. In contrast, the range-rate spread for the zero-Doppler flight remains for a longer period. The spread in range-rate in this case is a result of the vortices interacting with the chaff cloud, which is observed due to the different aspect angle. The velocities of the chaff are initially high since they are located closer to the vortex cores, but are reduced when moved further from the cores, see figure 4.2. Common for both scenarios is the fact that the RCS values are lower than real values. Both scenarios show a similar trend to the one proposed in (3.2), and has a behaviour similar to a Swerling model. However, both scenarios give a low overall RCS value which is likely due to insufficient diffusion modelling.

Another problem with the individual chaff model is slow run-time. Simulating fours seconds in the video generator takes an estimated 2-3 hours, which is not ideal. However, running the model outside of the video generator results in a much lower run-time. Simulating one minute outside the video generator takes a little more than a minute. Since the video generator also generates signal data it is much slower. Currently, not much effort has been made to optimize the model code.

5.2 Gaussian Model

Since it was not possible to adapt the Gaussian model to real recorded data due to confidentiality, the results from the individual chaff model were used instead. The results can be seen in appendix A, since they are very similar to the results from the individual chaff model. When compared, the Gaussian model follows the same type of trends as the individual chaff model. Hence, the model seems to be able to follow data successfully.

The Gaussian model run-time is much lower than the individual chaff model. Simulating four seconds takes around 30 minutes. This is due to the fact that the Gaussian model uses trends and pre-adapted values, which requires fewer simulated chaff. Hence, the video generator can generate signals faster.

Chapter 6
Future Work

In this thesis, two chaff models were created. The natural next step would be to compare the models with recorded data from actual flight tests. Due to the confidential nature of this subject, there is a lack of both public articles and data. There were data available at SAAB but due to confidentiality, no such comparison could be made.

For the individual chaff model, it would be interesting to know how the range-Doppler plots differ depending on flight scenario and how much the wing-tip vortices actually contribute to the spread in range-rate. For the Gaussian model, one could investigate whether the exponential trends used for RCS, positions and velocities correspond to a real situation. Currently, the Gaussian model has not been validated properly since there was no access to real data. The idea was to create a statistical model based on recorded data. Such a model would be sufficient in simulating already known behaviour and be useful for testing signal processing algorithms. The model would however not be able to investigate new, previously unknown, behaviour. A vision for a future chaff model is the possibility to pre-define flight manoeuvrers and to be able to investigate how the airplane movement affects the behaviour of the chaff cloud. This was the philosophy behind the individual chaff model.

In the individual chaff model there are quite a few simplifications and thus room for improvement. One of the biggest flaws with the simulation is the lack of diffusion and turbulence. This heavily affects the dispersion of the cloud and resulted in low RCS values, small cloud sizes and a small range spread. A simple way of introducing turbulence to the model would be to add random velocities, as described in section 3.1.4. The convection-diffusion model attempted to simulate the diffusion aspects of the chaff cloud, but proved to be too computer heavy and was not proceeded further. However, the model showed interesting preliminary results. Continued work could include an attempt at only modelling the convection-diffusion radially in 2D, thus reducing the computing time.

Regardless of modelling approach, more theoretical work is needed to better understand the diffusion effects and the turbulence causing the dispersion. Since the near-field is heavily affected by turbulence, properly modelling it is difficult since turbulence is a notoriously difficult phenomena to simulate [37]. In the individual chaff model, only two vortices were simulated with the assumption that the entire circulation Γ was conserved. The fact that there are multiple small vortices from an airplane body which combine into larger vortices during the roll-up

process has not been taken into account. Continued and more thorough investigations of the aerodynamics and the wake vortices in the near-field are required, which would also require more advanced simulating software. Several such software exist, such as TORNADO written in MATLAB by Thomas Melin [38], which uses a text based interface for linear aerodynamic wing design applications. Different wing types and airframes can be modelled. Afterwards, a flight state can be defined, changing for example the angle of attack, wind speed and altitude of the airplane. When the state has been defined, TORNADO solves aerodynamic equations and the results are presented, such as the positions of the vortices and their Γ values. However, TORNADO does not model the wake or the Γ values of the wing-tip vortices. Attempts at using TORNADO were made during the thesis. Unfortunately, it proved more difficult than originally thought to apply the values from the simulation with the simplified model created. Properly using the Γ values produced by the TORNADO and implementing them in the current, or more advanced models, would be interesting.

TORNADO or more advanced aerodynamics software such as EDGE, which is the aerodynamics software used at SAAB, would preferably be used to improve the simulation of the wake turbulence and the wing-tip vortices. Using such software would also allow simulating the airplane at specific flight states and changing parameters such as the angle of attack, which has a large impact on the strengths in the wing-tip vortices. In the individual chaff model, it is possible to change a few parameters, such as mass of the airplane, wing-span and position of the chaff cartridges. In the future, the cloud behaviour could be investigated by changing these parameters as well. The load factor was the only parameter change which was investigated, as seen in figure 5.13.

Another method is using Large eddy simulation proposed by Mengda Lin et al. in [32]. Combining this with an investigation on more advanced particle models, to simulate the chaff interaction with the turbulence and vortices, could be done. This would likely require a large amount of computer time due to the advanced computations. Another issue with such a model would be that since the radar has a limited resolution, there may not be an advantage in actually performing such calculations. If the range resolution of the radar is 1 m, there would perhaps be no need in simulating every individual chaff, which are only a few centimetres in size. Furthermore, it may not be necessary to simulate the cloud for a longer time than the signal processing algorithms need to distinguish a real target from a chaff cloud. Since the processing time is usually only a few milliseconds, there may not be a need to simulate the cloud for four seconds as done in this thesis.

The radar echoes are calculated as a sum of point targets or so called virtual scatterers. This is highly time consuming method of generating a signal as it requires roughly 50 scatterers to achieve realistic results. It would be interesting to investigate different signal generation methods such as using the convolution of the transmitted signal with the impulse response of the cloud, as described in [39]. Similarly, the RCS is calculated by only using the geometric cross-section. Without any proper diffusion, an increase in the amount of simulated chaff do not result in a higher RCS value. Investigating whether the reflectivity and directivity have an impact would also be necessary.

Chapter 7

Summary and Conclusions

This master thesis was a pilot study on how chaff interact with wing-tip vortices in the near-field to create chaff clouds. The aims for the project were:

- Conduct a literature study to investigate existing chaff models including the effect of wing-tip vortices.
- Create a model in MATLAB simulating the aerodynamic and spectral characteristics of a chaff cloud.
- The model should generate input to existing signal processing methods that analyse Doppler spectra of chaff clouds.

A literature study was conducted to investigate the current open publications on chaff cloud simulations with wing-tip vortices, but findings were scarce. The majority of the articles had focused on modelling chaff clouds without the interaction of any aerodynamics from an airplane. Furthermore, the articles did not include any thorough comparisons with recorded data. Some success was found internally at SAAB however, where a basic model had been previously created which simulated six chaff strips affected by wing-tip vortices.

Based on these findings, two simple models are created, the individual chaff model and the Gaussian model. They have two separate approaches. The individual chaff model is heavily based on the model previously created at SAAB. It has a physical approach and tries to simulate wing-tip vortices created by an airplane in the near-field. The vector field created by the vortices is used to model the trajectories of individual chaff over time, creating a basic simulation of how chaff are dispersed in the wake of an airplane. The second model, the Gaussian model, has a statistical approach. It is based on many of the previous models found in publicly available articles. Instead of modelling physical behaviours, this model is meant to be adapted to existing data by using trends and standard deviations of the chaff velocities, positions and RCS. They were both implemented in a program used for signal processing at SAAB, and can thus be used to produce test data. However, the models are currently very slow, especially the individual chaff model.

Unfortunately, it was not possible to compare the results with real data, due to confidentiality. Instead, two flight scenarios were tested for the individual chaff model and compared to trends found in articles. One where the radar recorded the chaff cloud from straight flight, and the other in zero-Doppler, perpendicular

to the flight direction. To test the Gaussian model, its parameters were adapted to the results from the individual chaff model. Both models showed promising results. The individual chaff model was able to simulate two separate scenarios with distinguishable results. This behaviour was also mimicked by the Gaussian model when adapted to the data. However, since no comparison could be made with real data, it is not known if these behaviours represent real life situations. Comparing with articles, both the RCS trends as well as the statistical behaviour agreed quite well. The RCS values were low, likely due to the individual chaff model not being able to model diffusion satisfactory.

Even though the models were successfully implemented, much more work is needed. Comparing with real data is the next natural step, since without it no real conclusions can be drawn whether the models are realistic or not. More work is also needed to understand the underlying phenomena which contribute to the chaff cloud diffusion. At this moment, exactly how the chaff clouds are created is not known. Advanced aerodynamics software could be used to better simulate the creation of wing-tip vortices and wake turbulence, in an effort to create a more realistic chaff cloud.

Bibliography

[1] Vakin, S. A. et al., *Fundamentals of Electronic Warfare*. Artech House, Inc, 2001.

[2] Wikimedia Commons, "File:usnchaff.jpg — wikimedia commons, the free media repository," 2016 (Last accessed 2019-02-07). `https://commons.wikimedia.org/w/index.php?title=File:Usnchaff.jpg&oldid=225236005`.

[3] GlobalSecurity.org, "Flares - Infrared Countermeasures," (Last accessed 2019-03-11). `https://www.globalsecurity.org/military/systems/aircraft/systems/flares.htm`.

[4] Wikimedia Commons, "File:c-130 hercules 10.jpg — wikimedia commons, the free media repository," 2017 (Last accessed 2019-02-07). `https://commons.wikimedia.org/w/index.php?title=File:C-130_Hercules_10.jpg&oldid=238117996`.

[5] Stimson, G. W., *Introduction to Airborne Radar, Second Edition*. SciTech Publishing, Inc, 1998.

[6] Nathanson, F. E. et al., *Radar Design Principles, Second Edition*. SciTech Publishing, Inc, 1991.

[7] Thorson, T. J., *Simultaneous Range-Velocity Processing and SNR Analysis of AFIT's Random Noise Radar*. [Master's Thesis]. Department of the Air Force, Air Force Institute of Technology, Wright-Patterson Air Force Base, Ohio, 2012 (Last accessed 2019-03-11). `https://apps.dtic.mil/dtic/tr/fulltext/u2/a556656.pdf`.

[8] Koks, D., *How to Create and Manipulate Radar Range-Doppler Plots*. Australian Government, Department of Defence, Defence Science and Technology Organisation, 2014 (Last accessed 2019-01-30). `https://apps.dtic.mil/dtic/tr/fulltext/u2/a615308.pdf`.

[9] B. C. F. Butters, "Chaff," *IEE Proceedings F - Communications, Radar and Signal Processing (Volume: 129, Issue: 3, June 1982)*, pp. 197–201, 1982. IEEE.

[10] Arnott, W. P. et al., "Determination of radar chaff diameter distribution function, fall speed, and concentration in the atmosphere by use of the NEXRAD radar," 2004. Desert Research Institute.

[11] Allen, J. L. and Diamond, B. L., *Mutual Coupling in Array Antennas*. Lincoln Laboratory, Massachusetts Institute of Technology, 1966 (Last accessed 2019-02-20). https://apps.dtic.mil/dtic/tr/fulltext/u2/648153.pdf.

[12] Wickliff, R. and Garbacz, R., "The average backscattering cross section of clouds of randomized resonant dipoles," *IEEE Transactions on Antennas and Propagation (Volume: 22, Issue: 3, May 1974)*, pp. 503–505, 1974. IEEE.

[13] Budge Jr, M. C., *Radar cross section*. University of Alabama in Huntsville, 2011 (Last accessed 2019-03-03). http://www.ece.uah.edu/courses/material/EE619-2011/RadarCrossSection(5)2011.pdf.

[14] M. C. Budge, Jr. and S. R. German, *Basic Radar Analysis*. Artech House, 2015.

[15] Näsvall, A. Skype meeting at SAAB, 2018-12-04.

[16] Xing, L., "Simulation of 3d advection-diffusion equation of pollutants on arbitrary polyhedron grids," *Conference on Environmental Pollution and Public Health*, 2010. Scientific Research Publishing.

[17] Wikimedia Commons, "File:forces2.gif — wikimedia commons, the free media repository," 2014 (Last accessed 2019-02-07). https://commons.wikimedia.org/w/index.php?title=File:Forces2.gif&oldid=142062817.

[18] NASA, *Four Forces on an Airplane*, (Last accessed 2019-02-07). https://www.grc.nasa.gov/www/k-12/airplane/forces.html.

[19] Larsson, R. Skype meeting at SAAB, 2018-12-07.

[20] Clancy, L. J., *Aerodynamics*. Pitman Publishing Limited, 1975.

[21] NASA, *Inclination Effects of Lift*. Glenn Research Center, 2018 (Last accessed 2019-03-20). https://www.grc.nasa.gov/WWW/k-12/airplane/incline.html.

[22] Houghton, E.L. and Carpenter, P.W., *Aerodynamics for Engineering Students, Fifth Edition*. Butterworth-Heinemann, 2003.

[23] NASA, *The Drag Equation*, (Last accessed 2019-02-07). https://www.grc.nasa.gov/www/k-12/airplane/drageq.html.

[24] NASA, *Three-Phased Wake Vortex Decay*, (Last accessed 2019-02-07). https://ntrs.nasa.gov/archive/nasa/casi.ntrs.nasa.gov/20100030583.pdf.

[25] Wikimedia Commons, "File:tip vortex rollup.png — wikimedia commons, the free media repository," 2016 (Last accessed 2019-02-07). https://commons.wikimedia.org/w/index.php?title=File:Tip_vortex_rollup.png&oldid=222753960.

[26] Puoliguen, P., "Simulation of chaff cloud radar cross section," *2005 IEEE Antennas and Propagation Society International Symposium*, 2005. IEEE.

[27] Ducata, D.D. et al., "A comprehensive model for chaff characterization," *2009 European Radar Conference (EuRAD)*, pp. 485–488, 2009. IEEE.

[28] Kaydok, U., "Baseband signal modelling of chaff echoes for coherent pulsed radars," *2018 IEEE Radar Conference (RadarConf18)*, pp. 0642 – 0646, 2018. IEEE.

[29] Bendayan, M. and Garcia, A., "Signal modeling of chaff in naval environment simulation," *IEEE Transaction on Aerospace and Electronic Systems (Volume: 51, Issue: 4)*, pp. 3161–3166, Oct 2015. IEEE.

[30] Hallock, J. N. and Eberle, W. R., *Aircraft Wake Vortices: A State-of-the-Art Review of the United Stated R&D Program.* U.S. Department of Transportation, Transportation Systems Center, 1977 (Last accessed 2019-02-12). `https://apps.dtic.mil/dtic/tr/fulltext/u2/a042442.pdf`.

[31] Chow, J. et al., "Turbulence measurements in the near field of a wingtip vortex," *NASA Technical Memorandum 110418*, 1997. NASA.

[32] Lin, M. et al., "A new vortex sheet model for simulating aircraft wake vortex evolution," *Chinese Journal of Aeronautics. Vol 30, Issue 4*, 2017. CSAA.

[33] Jasinski, T. and Cooke, M. Australian Government, Department of Defence, Defence Science and Technology Organisation.

[34] Sedin, Y. C-J et al., "A model for simulation of flight passages through trailing tip vortices," *ICAS 2002 Congress*, 2002. International Council of the Aeronautical Sciences.

[35] Näsvall, A., "Simulering av molnuppväxt i närzonen bakom flygplan," 1982. [Saab internal report M-10091328].

[36] Xiang, H. and Feng-ju, K., "The visualization simulation of chaff based on aerodynamics and statistics," *2009 Third International Symposium on Intelligent Information Technology Application*, 2009. IEEE.

[37] Clay Mathematics Institute, "Millennium problems," (Last accessed 2019-03-10). `http://www.claymath.org/millennium-problems`.

[38] Melin, T., *Tornado A Vortex Lattice Method implemented in MATLAB.* Glenn Research Center, NASA, (Last accessed 2019-02-03). `https://tornado.redhammer.se/`.

[39] Seltzer, J. E., *Response of an airborne-short-pulse radar to chaff.* Harry Diamond Laboratories, 1972 (Last accessed 2019-01-30). `https://apps.dtic.mil/dtic/tr/fulltext/u2/744776.pdf`.

Appendix A

Gaussian Model Results

A.1 Gassian Model Curve Fitting

Figures A.1-A.6 show data generated from the individual chaff model in the straight flight scenario as well as fitted curves based on (4.4), (4.7) and (4.8). The variable values are shown in the captions and are used to generate the data in figures A.7-A.12.

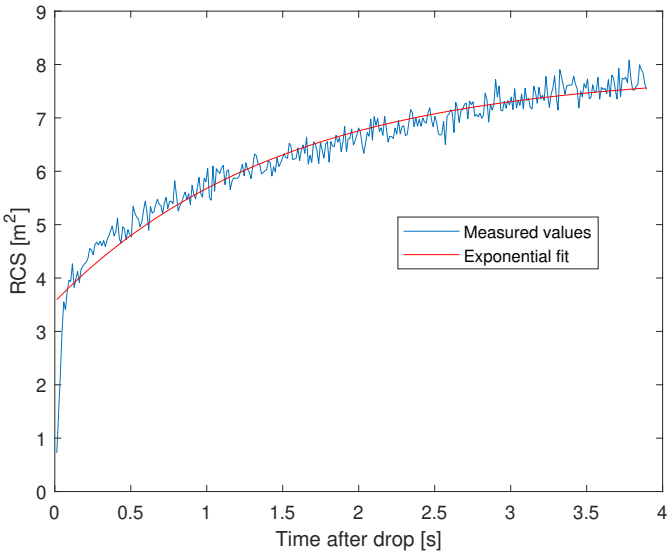

Figure A.1: Measured RCS values and an exponential fit based on (4.8). The equation of the exponential fit is $f(t) = -4.31 \cdot \exp(-0.677 \cdot t) + 7.87$.

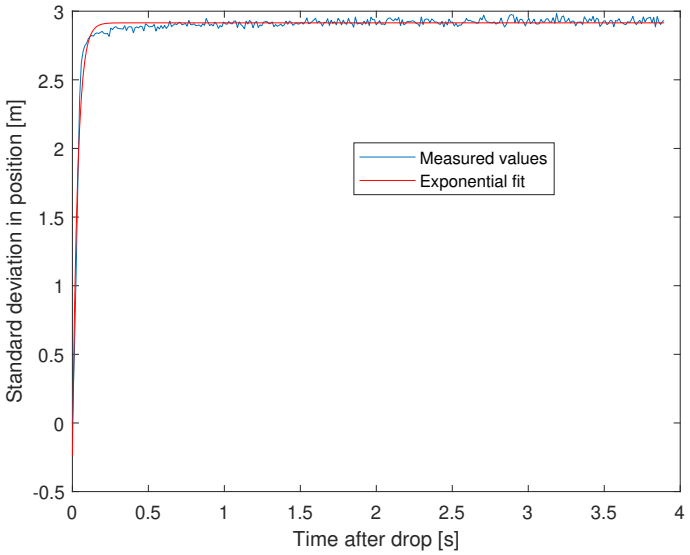

Figure A.2: Measured standard deviation in position along the x-axis and an exponential fit based (4.7). The equation of the exponential fit is $f(t) = -3.15 \cdot \exp(-29.8 \cdot t) + 2.91$.

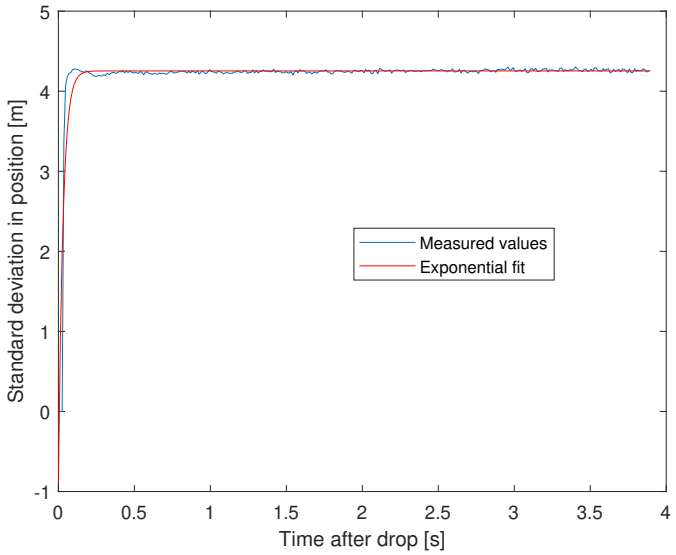

Figure A.3: Measured standard deviation in position along the y-axis and an exponential fit based on (4.7). The equation of the exponential fit is $f(t) = -5.14 \cdot \exp(-33.0 \cdot t) + 4.25$.

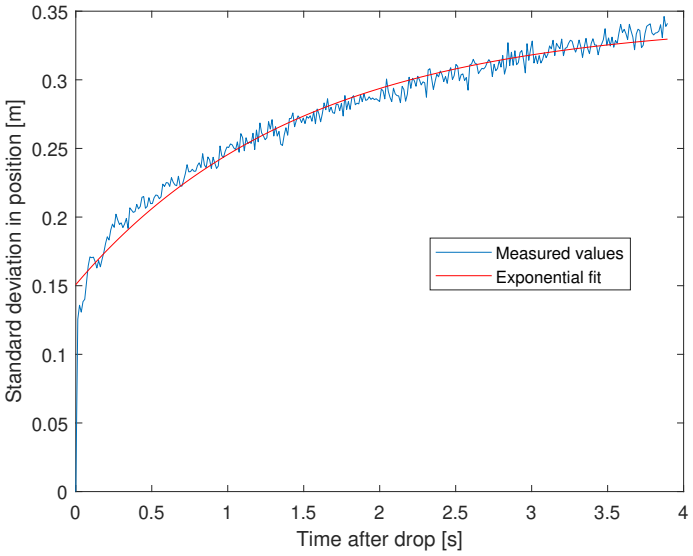

Figure A.4: Measured standard deviation in position along the z-axis and an exponential fit based on (4.7). The equation of the exponential fit is $f(t) = -0.193 \cdot \exp(-0.676 \cdot t) + 0.343$.

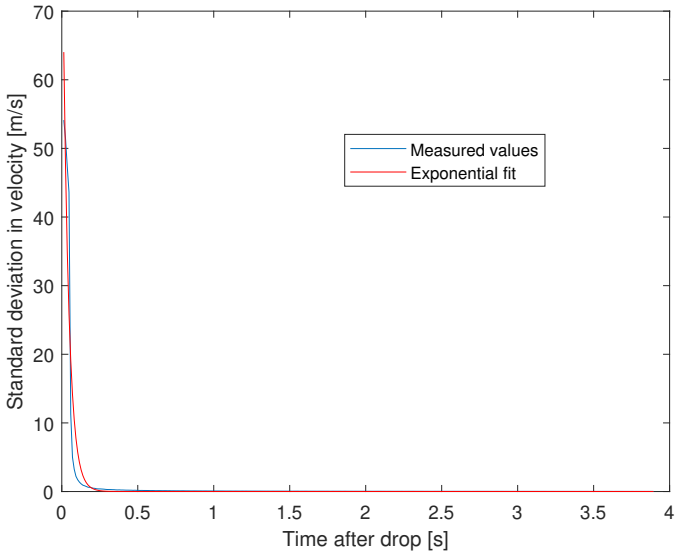

Figure A.5: Measured standard deviation in velocity along the x-axis and an exponential fit based on (4.4). The equation of the exponential fit is $f(t) = 90.8 \cdot \exp(-26.4 \cdot t) + 0.00809$.

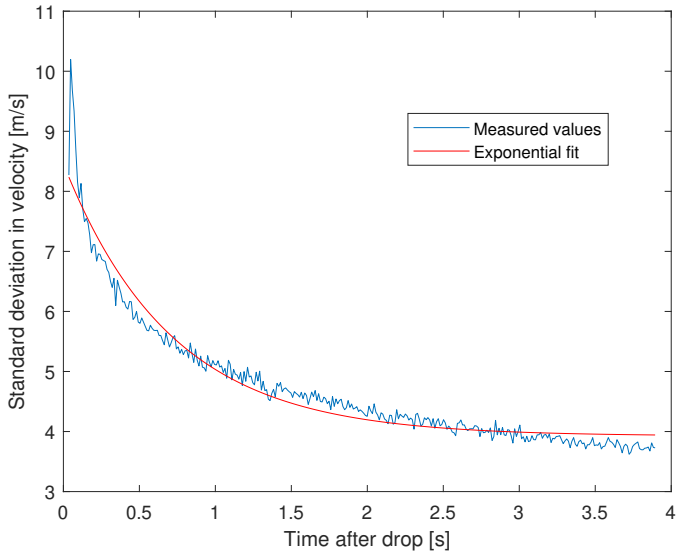

Figure A.6: Measured standard deviation in velocity along the y-axis and an exponential fit based on (4.4). The equation of the exponential fit is $f(t) = 4.53 \cdot \exp(-1.41 \cdot t) + 3.92$. The same curve was also used for the standard deviation in velocity along the z-axis.

A.2 Straight flight

Range-Doppler Plots

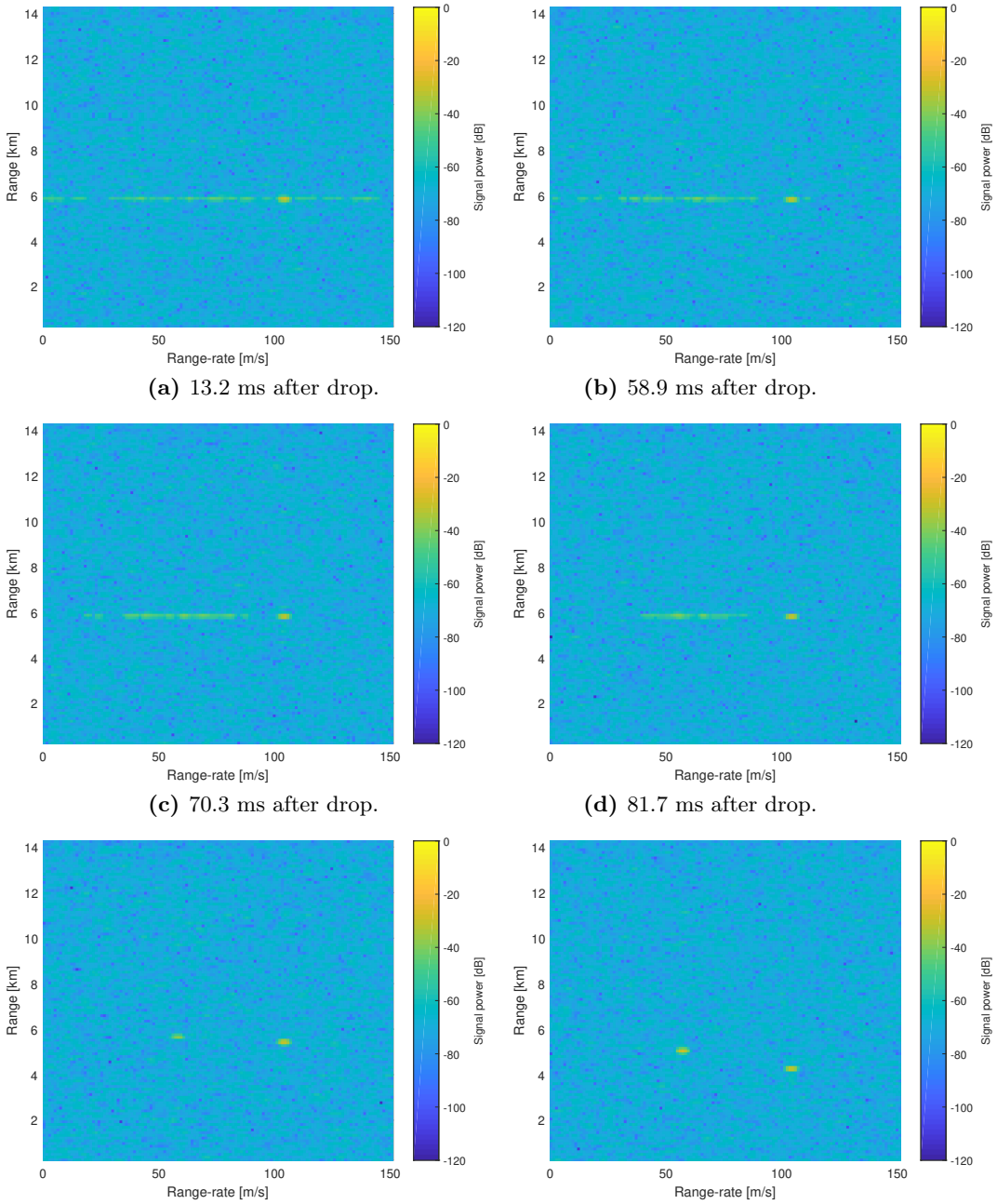

(a) 13.2 ms after drop.

(b) 58.9 ms after drop.

(c) 70.3 ms after drop.

(d) 81.7 ms after drop.

(e) 1017.7 ms after drop.

(f) 3894.1 ms after drop.

Figure A.7: Range-Doppler spectra from straight flight at different times.

Range Distributions

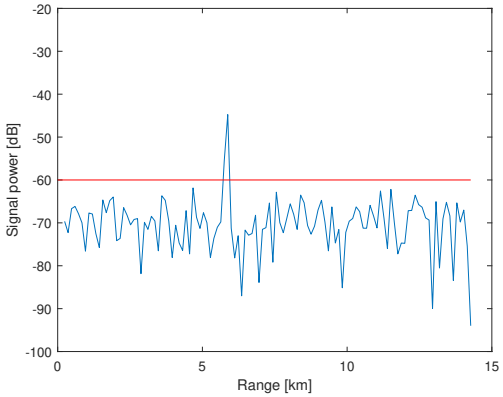

(a) Range distribution at 63.08 m/s, 13.2 ms after drop.

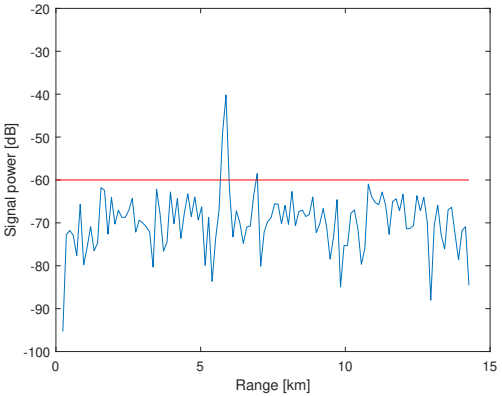

(b) Range distribution at 63.08 m/s, 58.9 ms after drop.

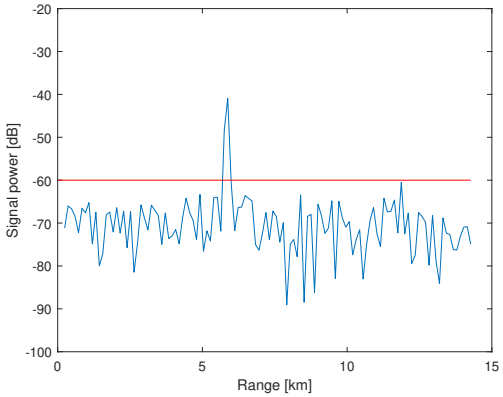

(c) Range distribution at 60.7 m/s, 70.3 ms after drop.

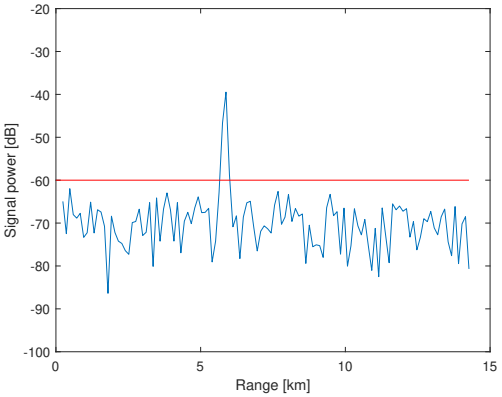

(d) Range distribution at 55.93 m/s, 81.7 ms after drop.

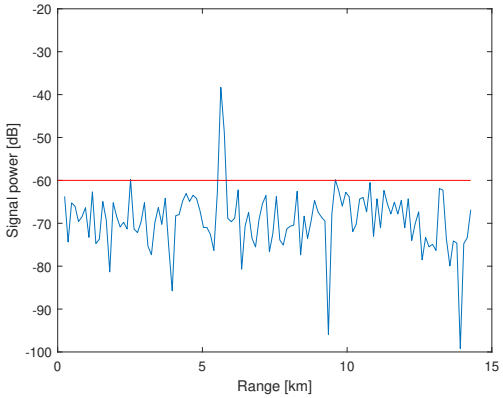

(e) Range distribution at 58.32 m/s, 1017.7 ms after drop.

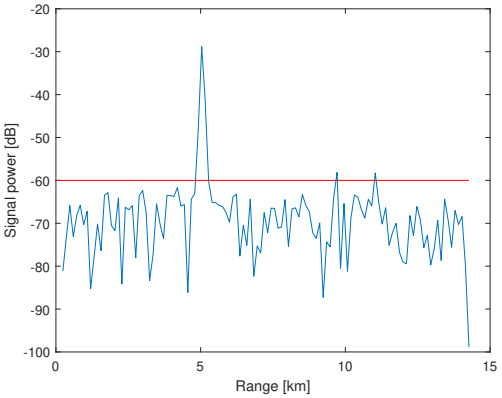

(f) Range distribution at 57.13 m/s, 3894.1 ms after drop.

Figure A.8: Range distributions at different range-rates and times for straight-flight.

Range-Rate Distributions

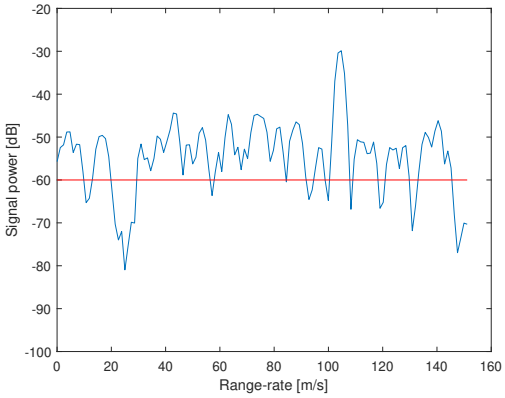

(a) Range-rate distribution at 5876 m, 13.2 ms after drop.

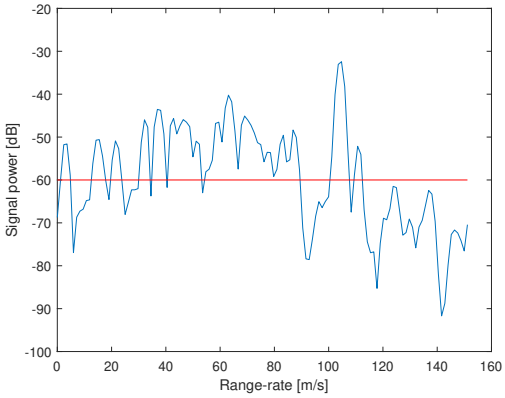

(b) Range-rate distribution at 5876 m, 58.9 ms after drop.

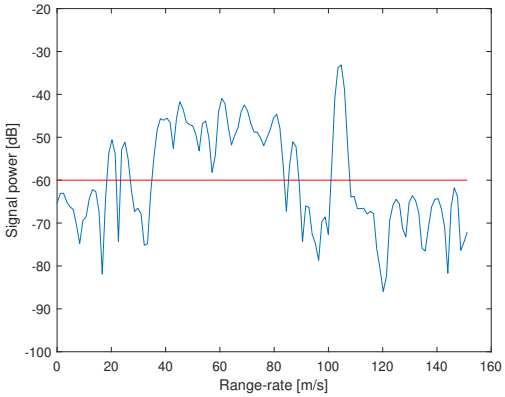

(c) Range-rate distribution at 5876 m, 70.3 ms after drop.

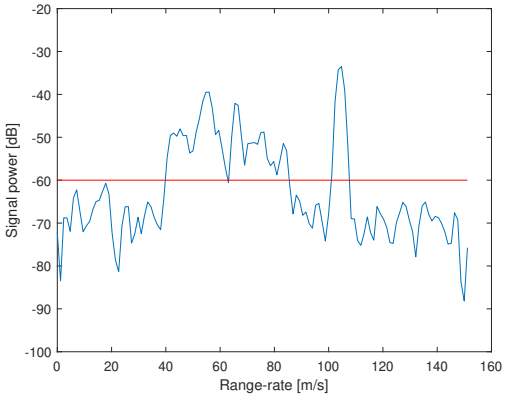

(d) Range-rate distribution at 5876 m, 81.7 ms after drop.

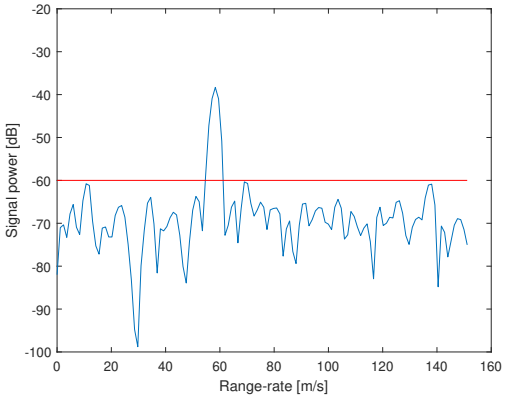

(e) Range-rate distribution at 5636 m, 1017.7 ms after drop.

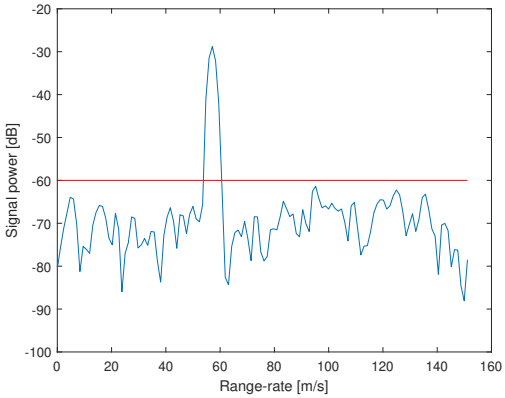

(f) Range-rate distribution at 5037 m, 3894.1 ms after drop.

Figure A.9: Range-rate distributions at different ranges and times for straight-flight.

A.3 Zero-Doppler Flight

Range-Doppler Plots

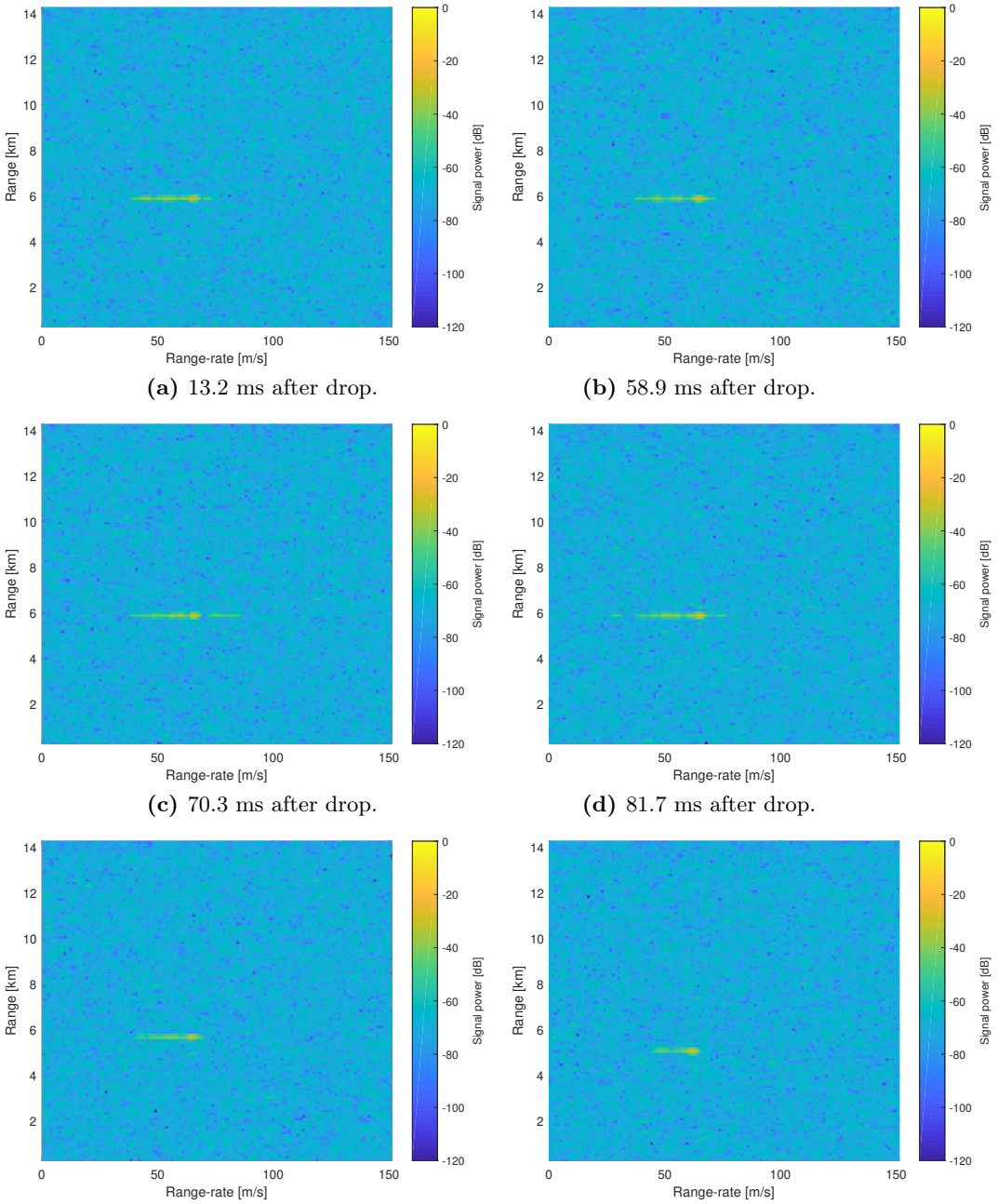

(a) 13.2 ms after drop.

(b) 58.9 ms after drop.

(c) 70.3 ms after drop.

(d) 81.7 ms after drop.

(e) 1017.7 ms after drop.

(f) 3894.1 ms after drop.

Figure A.10: Range-Doppler spectra from zero-Doppler flight at different times.

Range Distributions

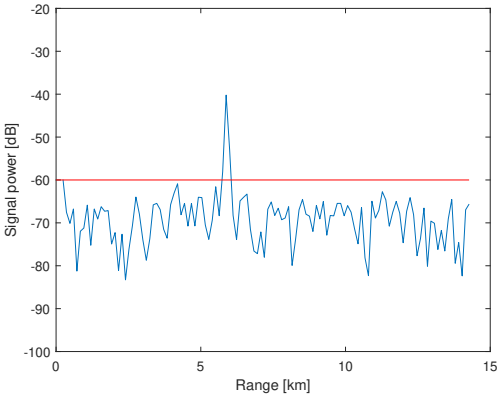

(a) Range distribution at 52.36 m/s, 13.2 ms after drop.

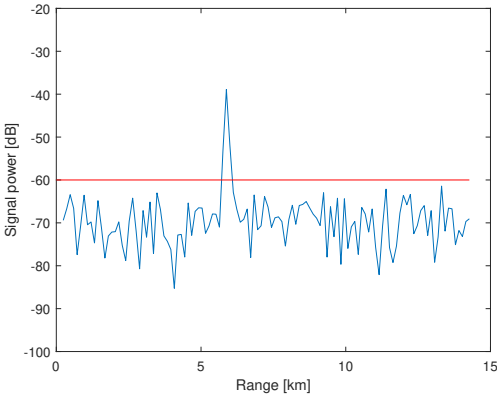

(b) Range distribution at 47.6 m/s, 58.9 ms after drop.

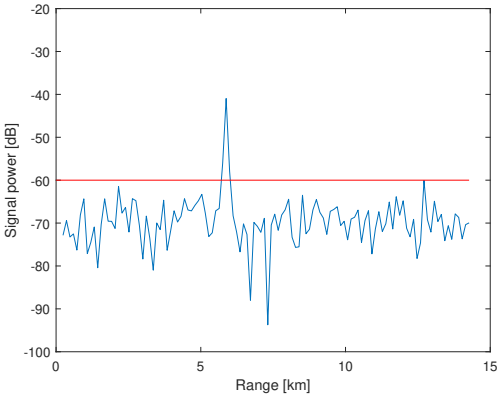

(c) Range distribution at 57.13 m/s, 70.3 ms after drop.

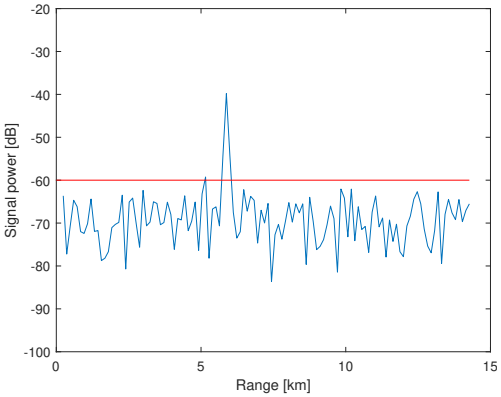

(d) Range distribution at 51.17 m/s, 81.7 ms after drop.

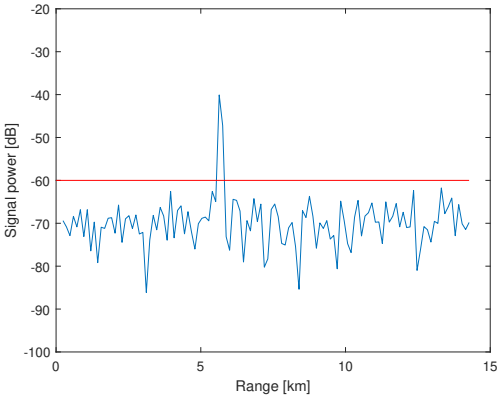

(e) Range distribution at 57.13 m/s, 1017.7 ms after drop.

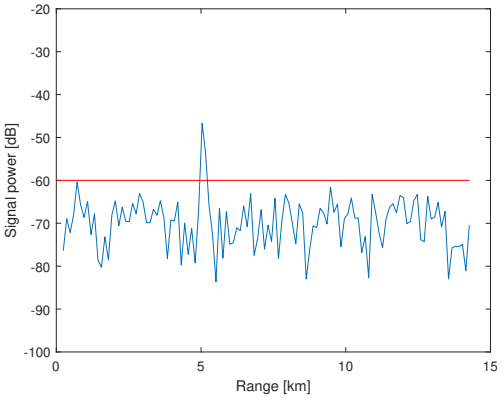

(f) Range distribution at 51.17 m/s, 3894.1 ms after drop.

Figure A.11: Range distributions at different range-rates and times for zero-Doppler flight.

Range-Rate Distributions

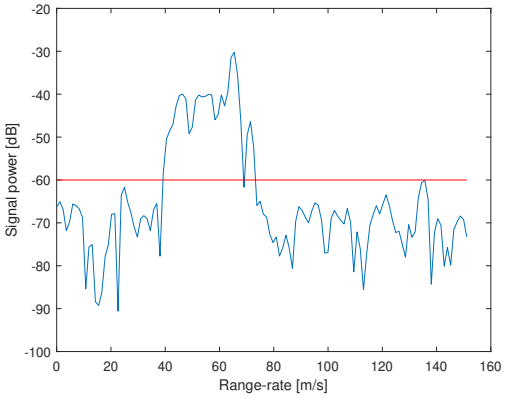

(a) Range-rate distribution at 5876 m, 13.2 ms after drop.

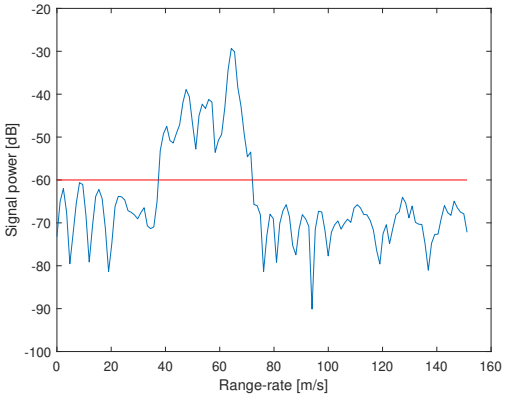

(b) Range-rate distribution at 5876 m, 58.9 ms after drop.

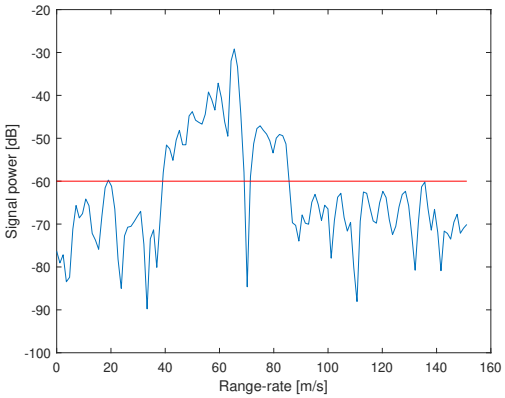

(c) Range-rate distribution at 5876 m, 70.3 ms after drop.

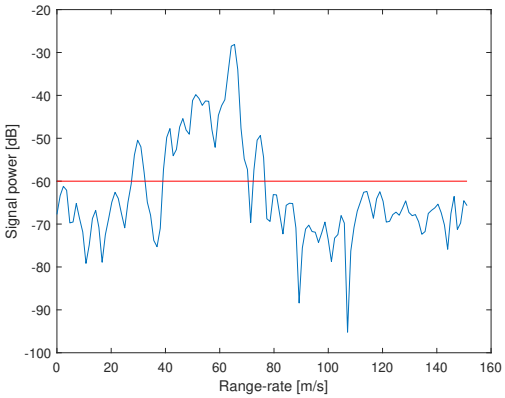

(d) Range-rate distribution at 5876 m, 81.7 ms after drop.

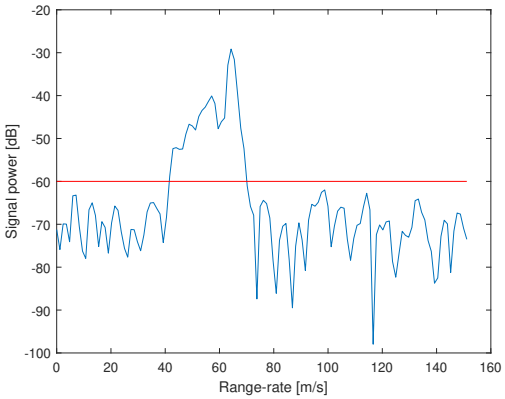

(e) Range-rate distribution at 5636 m, 1017.7 ms after drop.

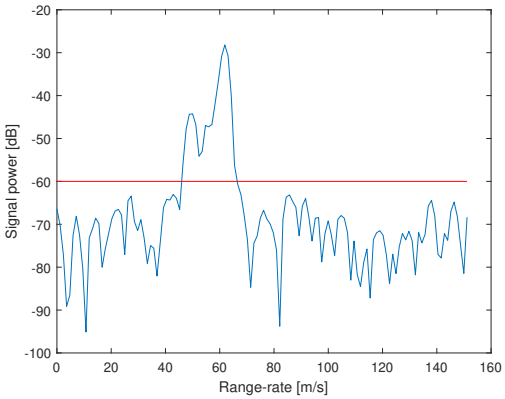

(f) Range-rate distribution at 5037 m, 3894.1 ms after drop.

Figure A.12: Range-rate distributions at different ranges and times for zero-Doppler flight.